Rotavirus Calcium Dysregulation Manifests as Dynamic Calcium Signaling in the Cytoplasm and Endoplasmic Reticulum

Alexandra L. Chang-Graham[1], Jacob L. Perry[1], Alicia C. Strtak[1], Nina K. Ramachandran[1], Jeanette M. Criglar[1], Asha A. Philip[3], John T. Patton[3], Mary K. Estes[1,2], and Joseph M. Hyser[1]*

[1]Alkek Center for Metagenomic and Microbiome Research; Department of Molecular Virology and Microbiology; [2]Department of Medicine, Gastroenterology and Hepatology, Baylor College of Medicine, Houston, TX 77303. [3]Department of Biology, Indiana University, Bloomington, IN 47405

*Correspondence should be sent to:
Joseph M. Hyser
Alkek Center for Metagenomic and Microbiome Research
Department of Molecular Virology and Microbiology
MS: BCM385
Baylor College of Medicine
Houston, TX, 77303
PH: 713-798-4514
FAX: 713-798-3586
Joseph.Hyser@bcm.edu

No conflicts of interest exist.

28 **Abstract**

29 Like many viruses, rotavirus (RV) dysregulates calcium homeostasis by elevating

30 cytosolic calcium ($[Ca^{2+}]$cyt) and decreasing endoplasmic reticulum (ER) stores. While

31 an overall, monophasic increase in $[Ca^{2+}]$cyt during RV infection has been shown, the

32 nature of the RV-induced aberrant calcium signals and how they manifest over time at

33 the single-cell level have not been characterized. Thus, we generated cell lines and

34 human intestinal enteroids (HIEs) stably expressing cytosolic and/or ER-targeted

35 genetically-encoded calcium indicators to characterize calcium signaling throughout RV

36 infection by time-lapse imaging. We found that RV induces highly dynamic $[Ca^{2+}]$cyt

37 signaling that manifest as hundreds of discrete $[Ca^{2+}]$cyt spikes, which increase during

38 peak infection. Knockdown of nonstructural protein 4 (NSP4) attenuates the $[Ca^{2+}]$cyt

39 spikes, consistent with its role in dysregulating calcium homeostasis. RV-induced

40 $[Ca^{2+}]$cyt spikes were primarily from ER calcium release and were attenuated by

41 inhibiting the store-operated calcium entry (SOCE) channel Orai1. RV-infected HIEs

42 also exhibited prominent $[Ca^{2+}]$cyt spikes that were attenuated by inhibiting SOCE,

43 underlining the relevance of these $[Ca^{2+}]$cyt spikes to gastrointestinal physiology and

44 role of SOCE in RV pathophysiology. Thus, our discovery that RV increases $[Ca^{2+}]$cyt

45 by dynamic Ca^{2+} signaling, establishes a new, paradigm-shifting understanding of the

46 spatial and temporal complexity of virus-induced Ca^{2+} signaling.

47

Introduction

Eukaryotic signal transduction pathways employ a variety of signaling molecules to regulate cellular processes. Calcium (Ca^{2+}) is one of the most ubiquitous secondary messengers in the cell, which tightly regulates Ca^{2+} movement through the coordinated function of Ca^{2+} channels, transporters, and pumps. Since Ca^{2+} signaling modulates a wide array of cellular processes, it is not surprising that many different viruses exploit Ca^{2+} signaling to facilitate their replication, and the resulting dysregulation of Ca^{2+} signaling causes pathogenesis. Rotavirus (RV), a member of the *Reoviridae* family, is one of the first viruses shown to elevate cellular Ca^{2+} levels and has become a widely-used model system to characterize mechanisms by which viruses dysregulate host Ca^{2+} homeostasis[1]. RV is a clinically important enteric virus that causes severe diarrhea and vomiting in children, resulting in over approximately 258 million diarrhea episodes and 198,000 deaths in 2016[2]. Hyperactivation of cyclic nucleotide (*e.g.*, cAMP/cGMP) and Ca^{2+} signaling pathways is a common strategy among enteric pathogens[3]. Thus, understanding how RV exploits Ca^{2+} signaling is key to understanding and combating RV-induced diarrhea.

RV was first reported to elevate cytosolic $[Ca^{2+}]$ by Michelangeli *et al.* (1991), which stimulated subsequent research into how RV alters cellular Ca^{2+} levels[4]. RV causes a 2-fold steady-state increase in cytosolic Ca^{2+}, which is due to increased Ca^{2+} release from the endoplasmic reticulum (ER) and increased Ca^{2+} influx through host Ca^{2+} channels in the plasma membrane (PM)[1,5]. Elevated cytosolic Ca^{2+} activates autophagy, which is critical for RV replication, and has wide-ranging consequences to

3

70   host cell functions, including disruption of the cytoskeleton and activation of chloride and

71   serotonin secretion to cause diarrhea and vomiting[1,5].

72   RV dysregulates Ca^{2+} homeostasis by at least two functions of its nonstructural

73   protein 4 (NSP4), a glycoprotein with multiple functions during the infection[5]. In RV-

74   infected cells, ER-localized NSP4 is a viroporin (*i.e.*, virus-encoded ion channel) that

75   releases ER Ca^{2+} and reduces ER Ca^{2+} stores causing a persistent increase in cytosolic

76   Ca^{2+} [6-8]. Using patch clamp electrophysiology, we demonstrated that the NSP4 viroporin

77   domain (aa47-90) forms a Ca^{2+}-permeable ion channel, confirming that NSP4 can

78   directly mediate loss of ER Ca^{2+} [9]. Decreased ER Ca^{2+} activates stromal interaction

79   molecule 1 (STIM1), an ER Ca^{2+} sensor, which in turn activates Ca^{2+} influx through

80   store-operated calcium entry (SOCE) channels in the PM, primarily Orai1[10]. Voltage-

81   gated Ca^{2+} channels and the sodium-calcium exchanger (NCX) have also been

82   implicated in Ca^{2+} influx in RV-infected cells[11,12]. Finally, through a mechanistically

83   distinct pathway, RV-infected cells secrete an extracellular NSP4 (eNSP4) cleavage

84   product that elicits a receptor-mediated, inositol triphosphate (IP_3)-dependent Ca^{2+}

85   signal [13,14]. eNSP4 induces diarrhea in neonatal mice, making this the first identified

86   viral enterotoxin [13,15]. At the cellular level, the eNSP4-induced Ca^{2+} signal activates

87   chloride secretion through Ca^{2+}-activated chloride channels (*e.g.*, anoctamin 1),

88   consistent with its enterotoxin activity *in vivo* [16,17]. Thus, NSP4 dysregulates Ca^{2+} by

89   both directly releasing ER Ca^{2+} and by exploiting host SOCE and agonist-induced Ca^{2+}

90   signaling pathways[1].

91   While the global dysregulation of Ca^{2+} homeostasis by RV has been well

92   characterized, many mechanistic details about RV-induced Ca^{2+} signaling remain

4

93   unknown. First, cell population-based studies show that RV induces a monophasic 2-

94   fold increase in cytosolic Ca^{2+} during infection[18,19], but whether individual cells manifest

95   this as a monophasic Ca^{2+} increase or a series of discrete Ca^{2+} signals remains

96   unknown. This is an important distinction because the amplitude, duration, and degree

97   of oscillation of cytosolic Ca^{2+} signals regulate downstream pathways. For example, a

98   sustained increase in cytosolic Ca^{2+} activates apoptotic programs, whereas transient or

99   oscillating Ca^{2+} signals activate proliferation and pro-survival pathways[20,21]. Second,

100 studies in single RV-infected cells have focused on times late post-infection, 7-8 hours

101 post-infection (hpi)[7,11]. Thus, it is not known whether RV dysregulates Ca^{2+} signaling

102 early in infection or how dysregulation of Ca^{2+} homeostasis progresses during the

103 infection. Finally, RV-induced depletion of ER Ca^{2+} remains controversial due to

104 conflicting data. RV decreases agonist-induced release of ER Ca^{2+} and induces STIM1

105 activation, suggesting decreased ER Ca^{2+} levels[10,22]. However, greater uptake of

106 radioactive Ca^{2+} into ER stores has also been observed[7]. As with cytosolic Ca^{2+}, ER

107 Ca^{2+} levels are dynamic; yet RV-induced changes to ER Ca^{2+} and how this relates to

108 cytosolic Ca^{2+} signaling remain incompletely characterized.

109   Addressing these gaps-in-knowledge requires the ability to measure changes in

110 cytosolic and ER Ca^{2+} with single-cell resolution over many hours. For many years,

111 technical limitations of Ca^{2+} indicator dyes (*e.g.*, photobleaching, uneven loading, and

112 dye leakage) made single-cell measurements of Ca^{2+} signaling throughout the entire RV

113 infection not feasible. However, we recently developed the use of genetically-encoded

114 calcium indicators (GECIs) for the study of Ca^{2+} signaling in virus-infected cells [23].

115 GECIs are dynamic fluorescent protein-based Ca^{2+} sensors, and variants have been

5

116   developed for simultaneous Ca^{2+} measurements in multiple cellular compartments (*e.g.,*

117   cytoplasm and ER) [24]. The stability and targetability of GECIs provides the spatial and

118   temporal resolution needed to perform long-term live-cell Ca^{2+} imaging such that Ca^{2+}

119   signaling can be measured throughout a RV infection. The goal of this study was to use

120   cell lines and human intestinal enteroids (HIEs) stably expressing cytoplasmic and/or

121   ER-localized GECIs to define RV-induced Ca^{2+} signaling dynamics at the single-cell

122   level, and thereby gain new mechanistic insights into how RV dysregulates Ca^{2+}

123   homeostasis.

124 **Materials and Methods**

125 **Cells and rotaviruses.** MA104 cells (African green monkey kidney cells) and HEK293T

126 cells (ATCC CRL-3216) were cultured in high glucose DMEM supplemented with 10%

127 fetal bovine serum (FBS) and Antibiotic/Antimycotic (Invitrogen) at 37°C in 5% CO_2.

128 Rotavirus SA114F was produced from in-house stocks. Porcine strains OSUv and

129 OSUa were provided as a kind gift from Dr. Lennart Svennson [25], and the human strain

130 Ito was prepared as previously described [26]. Recombinant SA11 clone 3 expressing an

131 mRuby3 red fluorescent protein reporter downstream of NSP3 (SA11-mRuby) was

132 generated using a modified plasmid based reverse genetics (RG) system [27]. Briefly, the

133 NSP4 open reading frame (ORF) in the pt7/NSP3 plasmid was replated with an ORF

134 encoding NSP3 fused downstream to FLAG-tagged mRuby3. To promote the

135 translation of NSP3 and mRuby3 as separate proteins, we inserted a teschovirus 2A-

136 like stop-restart translation element between the NSP3 and FLAG-tagged mRuby3

137 coding sequences[28]. The SA11-mRuby virus was generated by co-transfection of BHK-

138 T7 cells with pT7 plasmids expressing RV plus-sense RNAs along with a plasmid

139 expressing the African swine fever virus NP868R capping enzyme from a CMV

140 promoter. All viruses were propagated in MA104 cells in serum-free DMEM

141 supplemented with 1 μg/mL Worthington's Trypsin, and after harvest stocks were

142 subjected to three freeze/thaw cycles and activated with 10 μg/mL Worthington's

143 Trypsin for 30 min at 37 °C prior to use.

144

145 **Chemicals.** 2-APB, KB-R7943 mesylate, BTP2 (YM 58483), and BAPTA-AM were

146 purchased from Tocris Bioscience. Methoxyverapamil (D600), nitrotetrazolium blue

7

147 (NBT), and BCIP were purchased from Sigma-Aldrich. Synta66 and GSK7975A were

148 purchased form Aobious. EGTA solution (0.5 M, pH 8.0) was purchased from

149 Invitrogen.

150

151 **Antibodies.** To detect RV, we used rabbit anti-RV strain Alabama [29] (IF, 1:80,000;

152 western blot, 1:3000), guinea pig anti-NSP2 [30] (IF, 1:5000), and rabbit anti-NSP4

153 aa120-147 [31] (western blot, 1:3000). Secondary antibodies for IF were donkey anti-

154 rabbit AlexaFluor 568 (Invitrogen) and donkey anti-guinea pig Dylight 549 (Rockland),

155 both at 1:2000. For western blots, we used mouse anti-GAPDH monoclonal antibody

156 (Lifetein) (1:5000) and secondary antibodies alkaline phosphatase-conjugated goat anti-

157 rabbit IgG or goat anti-mouse IgG (Southern Biotech) (1:2000).

158

159 **Calcium indicator lentiviruses, cell lines, and enteroids.** GCaMP5G (Addgene

160 plasmid #31788), GCaMP6s (Addgene plasmid #40753), and G-CEPIA1er (Addgene

161 plasmid #105012) were cloned into pLVX-Puro. RGECO1.2 (Addgene plasmid #45494),

162 R-CEPIA1er (Addgene plasmid #58216), and GCaMP6s were cloned into pLVX-IRES-

163 Hygro. Lentivirus vectors for the GECI constructs were packaged in HEK293T cells as

164 previously described [23] or produced commercially (Cyagen Biosciences, Inc.).

165 Production of the MA104-GCaMP5G and MA104-GCaMP5G/RCEPIAer cell lines were

166 previously described and similar methods were used to generate MA104-

167 RGECO1/GCEPIAer and the MA104-GCaMP6s-shRNA lines [23]. Human intestinal

168 enteroids expressing GCaMP6s (G6S-HIEs) were created using lentivirus transduction

8

169   as described previously and grown in high Wnt3a CMGF+ with 1 µg/mL puromycin for

170   selection[32]. Proper GECI functionality was validated by responses to 50 µM ATP.

171

172   **MA104-GCaMP6s cells expressing NSP4 shRNAs.** Lentivirus constructs encoding

173   shRNA targeting SA11 gene 10 and a non-targeting scrambled shRNA negative control

174   were generated and packaged by America Pharma Source, LLC. The NSP4-shRNA1

175   targets gene 10 nt50-70 (5'-GCTTACCGACCTCAATTATAC-3') and NSP4-shRNA2

176   targets gene 10 nt176-196 (5'-GCTACATAAAGCATCCATTCC-3'). The shRNA-

177   expression vectors encode a blasticidin-resistance gene for drug selection. Parental

178   MA104 cells were transduced with the shRNA-expressing constructs and at 72 hrs post-

179   transduction the cells were passaged in the presence of 30 µg/mL blasticidin to select

180   for stably transduced cells. These three cell lines were then transduced with GCaMP6s

181   GECI (in pLVX-IRES-Hygro) and passaged with 50 µg/mL hygromycin B and 30 µg/mL

182   blasticidin to select for co-expression of GCaMP6s and the shRNA.

183

184   **Establishment of HIE cultures.** Three-dimensional human intestinal enteroid (HIE)

185   cultures were generated from crypts isolated from adult patients undergoing bariatric

186   surgery as previously described[26,33]. These established cultures were obtained at Baylor

187   College of Medicine through the Texas Medical Center Digestive Diseases Center

188   Gastrointestinal Experimental Model Systems Core. For these studies, jejunum HIEs

189   from patient J3 were used. Complete media with and without growth factors (CMGF+

190   and CMGF-, respectively), differentiation media, and high Wnt3a CMGF+ (hW-CMGF+)

191   were prepared as previously described[26,33,34]. Fluorobrite DMEM supplemented with

9

192 15mM HEPES, 1X sodium pyruvate,1X Glutamax, and 1X non-essential amino acids

193 (Invitrogen) was used for fluorescence Ca^{2+} imaging (FB-Plus). An FB-Plus-based

194 differentiation medium (FB-Diff) consisted of FB-Plus with the same added components

195 as differentiation media, but without Noggin. HIEs were grown in phenol red-free,

196 growth factor-reduced Matrigel (Corning). G6S-jHIE monolayers were prepared from

197 three-dimensional cultures and seeded into optical-bottom 10-well Cellview chamber

198 slides coated with dilute collagen IV (Sigma) as described previously[35,36]. After 24 hr in

199 CMGF+ and 10 μM Y-27632 Rock inhibitor, differentiation medium was used and

200 changed every day for 4-5 days.

201

202 **Microscopy and image analysis.** To image viroplasms, we used a GE Healthcare

203 DeltaVision LIVE High Resolution Deconvolution with an Olympus IX-71 base and

204 illumination provided by a xenon lamp. Images were captured with Plan Apo 60X Oil

205 DIC objective and a pco.edge sCMOS camera. Images were acquired and deconvolved

206 using SoftWoRx software and further analyzed with Fiji (ImageJ).

207   For calcium imaging, MA104 cells and HIEs were imaged with a widefield

208 epifluorescence Nikon TiE inverted microscope using a SPECTRAX LED light source

209 (Lumencor) and either a 20x Plan Fluor (NA 0.45) phase contrast or a 20X Plan Apo

210 (NA 0.75) differential interference contrast (DIC) objective. Fluorescence and

211 transmitted light images were recorded using an ORCA-Flash 4.0 sCMOS camera

212 (Hamamatsu), and Nikon Elements Advanced Research v4.5 software was used for

213 multipoint position selection, data acquisition, and image analysis.

10

214   Images were read-noise subtracted using an average of 10 no-light acquisitions

215 of the camera. Single cells were selected as Regions of Interest (ROI) and fluorescence

216 intensity measured for the experiment. 3D HIE's fluorescence was measured

217 individually using threshold analysis adjusted to select each enteroid with the Fill Holes

218 algorithm included. Enteroids that moved out of the field of view or could not be

219 separated from adjacent enteroids were removed from analysis. The fluorescence

220 intensity of whole field-of-view was measured for HIE monolayers.

221   Fluorescence intensity values were exported to Microsoft Excel and normalized

222 to the baseline fluorescence. The number and magnitude of Ca^{2+} spikes were

223 calculated by subtracting each normalized fluorescence measurement from the previous

224 measurement to determine the change in GECI fluorescence (ΔF) between each

225 timepoint. Ca^{2+} signals with a ΔF magnitude of > 5% were counted as Ca^{2+} spikes.

226

227 **Calcium imaging.** *MA104-GECI cells.* Confluent monolayers of MA104-GECI cells in 8-

228 well chamber slides (ibidi) were mock- or RV-infected in FBS-free media for 1 hr at the

229 indicated multiplicity of infection (MOI). Then the inoculum was removed and replaced

230 with FB-Plus, and for appropriate studies, with DMSO or drugs at indicated

231 concentrations. The slide was mounted into an Okolab stage-top incubation chamber

232 equilibrated to 37°C with a humidified 5% CO_2 atmosphere. For each experiment, 3-5

233 positions per well were selected and imaged every 1 minute for ~18-20 hrs.

234 *GECI HIEs.* To test Ca^{2+} response, 3D G6S-jHIEs were suspended in 25% Matrigel

235 diluted in FB-Diff media and seeded into optical-bottom 10-well Cellview chamber slides

236 (Greiner bio-one) thinly coated with Matrigel. After baseline imaging using the stage-top

11

237   incubator, 200µM carbachol in FB-Diff or FB-Diff alone was added to the well and

238   imaging continued for 1 hour with 6-10 enteroids imaged every 10 s.

239   For RV infection in 3D HIEs, the jHIEs were split and grown in hW-CMGF+ for 2

240   days followed by differentiation medium for 1 day. G6S-jHIEs were gently washed using

241   ice cold 1XPBS and resuspended in inoculum of 50µL MA104 cell lysate or RV (strain

242   Ito) diluted with 150 µL CMGF- and incubated for 1 hr. Then HIEs were washed,

243   resuspended in 25% Matrigel diluted in FB-Diff (with DMSO or 2-APB in indicated

244   experiments) and pipetted onto 8-well chamber slides (Matek) pre-coated with Matrigel.

245   Imaging positions were chosen so that between 20-50 enteroids were selected per

246   experimental condition. Enteroids were imaged using the stage-top incubator with

247   transmitted light and GFP fluorescence every 2-3 minutes for ~18 hrs.

248   For RV infection in monolayers, G6S-jHIE monolayers were washed once with

249   CMGF- and treated with an inoculum of 50µL CMGF- plus 30µL MA104 cell lysate or

250   RV (strain Ito) and incubated for 2 hr. Then inoculum was removed, and monolayers

251   were washed once with FB-Diff before adding FB-Diff with DMSO or 2-APB. Monolayers

252   were transferred to the stage-top incubator for imaging with 4 fields of view chosen per

253   well, and GFP fluorescence was measured every minute for ~18 hrs.

254

255   **Store-operated calcium entry assay.** G6S-jHIE monolayers after 4 days in

256   differentiation media were washed and incubated in 0mM Ca^{2+} ($0Ca^{2+}$) Ringers solution

257   (160mM NaCl, 4.5mM KCl, 1mM $MgCl_2$, 10mM HEPES, pH=7.4). Endoplasmic

258   reticulum Ca^{2+} stores were depleted by incubating cells with 500nM thapsigargin in

259    $0Ca^{2+}$ with either 50 µM 2-APB or DMSO as a vehicle control. SOCE was measured

12

260 using live-cell fluorescence imaging of the increase in GFP fluorescence after the

261 addition of normal Ringers to bring the total Ca^{2+} concentration to 2mM.

262

263 **Western blot analysis.** RV proteins were detected by immunoblot analysis as

264 previously described, with the following modifications[31]. Cells were lysed using a 1X

265 RIPA buffer solution [10mM Tris-HCL pH 8.0, 1mM EDTA, 1% Triton X-100, 0.1%

266 sodium deoxycholate, 0.1% SDS, 140mM NaCl, and 1 tablet complete mini protease

267 inhibitor (Roche)] and passed through a Qiashredder (Qiagen). Samples were boiled for

268 10 min at 100°C in SDS-PAGE sample buffer and separated on Tris-glycine 4-20%

269 SDS-PAGE gels (BioRad). Detected protein bands for each blot were quantified using

270 ImageJ software for gel densitometry measurements of NSP4:GAPDH.

271

272 **Immunofluorescence.** MA104 cells and HIEs were fixed using the Cytofix/Cytoperm kit

273 (BD Biosciences) according to manufacturer instructions. Primary antibodies were

274 diluted in 1X Perm/Wash overnight at 4°C. The next day, the cells were washed three

275 times with 1X Perm/Wash solution and then incubated with corresponding secondary

276 antibodies for 1 hr at room temperature. Nuclei were stained with NucBlue Fixed Cell

277 Stain (Life Technologies) for 5 min at room temperature and washed with 1X PBS for

278 imaging.

279

280 **Plaque assays.** Plaque assays were performed as described previously with the

281 following modifications [37]. Briefly, MA104 cells or the MA104-shRNA expressing cells

282 were seeded and grown to confluency in 6 wells plates. Wells were infected at 10-fold

13

283   dilutions in duplicate for 1 hr and media replaced with an overlay of 1.2% Avicel in

284   serum-free DMEM supplemented with DEAE dextran, and 1µg/mL Worthington's

285   Trypsin, and, for indicated experiments, DMSO vehicle or SOCE drugs[38]. The cells were

286   incubated at 37°C/5% CO_2 for 48-72 hrs before overlay was removed and cells stained

287   with crystal violet to count plaques.

288

289   **RNA extraction, reverse transcription, and quantitative PCR.** Total RNA was

290   extracted from HIEs wells (in hW-CMGF+ or differentiation media for 4 days) or MA104

291   cells grown to confluency in a 6-well plate using TRIzol reagent (Ambion). Total RNA

292   was treated with Turbo DNase I (Ambion) and cDNA was generated from 250 ng RNA

293   using the SensiFAST cDNA synthesis kit (Bioline). Quantitative PCR was performed

294   using Fast SYBR Green (Life Technologies) with primers designed using NCBI Primer-

295   Blast (Table 1) and using a QuantStudio real time thermocycler (Applied Biosciences).

296   Target genes were normalized to the housekeeping gene ribosomal subunit 18s and

297   relative expression was calculated using the ddCT method.

298

299   **Statistical analysis.** Biostatistical analyses were performed using GraphPad

300   Prism (version 8.1) with results presented as mean ± standard deviation. Comparisons

301   used an unpaired Student's t-test, the nonparametric Mann-Whitney test, or a One-way

302   Analysis of Variance (ANOVA) with Tukey's post hoc multiple comparisons test where

303   appropriate. Differences were considered statistically significant for $p < 0.05$. All authors

304   had access to the study data, reviewed, and approved the final manuscript.

305

Results

306

307   Previous studies have shown that RV significantly increases cytosolic Ca^{2+} over

308   several hours during the peak of RV replication[18,39]; however, the kinetics of this

309   increase and whether it is a monophasic increases or manifests as discrete Ca^{2+}

310   transients are not known. To address these questions, we developed a series of cell

311   lines stably expressing GECIs and used these cell lines to perform live-cell Ca^{2+}

312   imaging over the course of a RV infection[23]. For the long-term imaging experiments,

313   MA104 cells stably expressing cytosolic GCaMP5G (MA104-GCaMP5G) were seeded

314   into chamber slides and either mock- or RV-infected with strain SA114F (MOI 10), and

315   GCaMP5G fluorescence imaged for ~18 hr (2-20 hpi) (Fig. 1). Mock-infected cells

316   maintained a low fluorescence throughout the time course (Fig. 1A, upper panels),

317   whereas RV-infected cells exhibited strongly increased fluorescence, indicating

318   elevated Ca^{2+} levels (Fig. 1A, lower panels and Supplementary Video 1 online). Since

319   GECIs use an engineered calmodulin to sense Ca^{2+}, overexpression of GCaMP5G

320   could act as a Ca^{2+} buffer and alter the kinetics of RV replication. To assess whether

321   the MA104-GCaMP5G cells exhibited altered RV infection/protein synthesis, we

322   analyzed NSP4 expression in parental MA104 cells and the MA104-GCaMP5G cells

323   infected with SA114F (MOI 10) from 3-8 hpi by western blot (Fig. 1B). NSP4 expression

324   was similar in both parental and GCaMP5G-expressing cells, indicating that stable

325   GCaMP5G expression does not interfere with RV infection.

326   Next, we measured changes in cytosolic Ca^{2+} by determining the relative

327   GCaMP5G fluorescence (F/F$_0$) for the whole field-of-view (FOV) (~455 μm^2) for three

328   replicate infections and time lapse images were acquired once per minute (Fig. 1C).

15

329   Mock-infected cells maintained low Ca^{2+} levels with few transient and low amplitude

330   Ca^{2+} signals (Fig. 1C, black and grey lines). In RV-infected cells, the steady-state Ca^{2+}

331   levels began to increase at ~6 hpi, and we observed many large amplitude, transient

332   Ca^{2+} signals that occurred concomitantly with the steady-state elevation in cytosolic

333   Ca^{2+} levels (Fig. 1C, arrow). Further, at 6-8 hpi the RV-infected cells had more low and

334   moderate amplitude Ca^{2+} signals than mock-infected cells (Fig. 1D, arrows), which

335   occurred during the initial increase in steady-state Ca^{2+} levels. A more detailed

336   examination of the Ca^{2+} signaling over a period of 5 mins at 480 minutes post-infection

337   (~8 hpi) shows that the increase in cytosolic Ca^{2+} manifests as discrete and dynamic

338   Ca^{2+} fluxes from individual or small groups of cells (Fig. 1E). The dynamic changes are

339   exemplified by the two areas outlined (Fig. 1E, magenta or yellow box), showing

340   substantial changes over the 5 min period. To compare our GECI-based Ca^{2+} imaging

341   of RV-induced Ca^{2+} signaling to previous cell population-based studies, we determined

342   the average GCaMP5G fluorescence from 18-19 hpi (Fig. 1F) and the slope of the

343   fluorescence increase from 8-18 hpi (Fig. 1G). We found a similar ~2-fold increase in

344    $[Ca^{2+}]c$ and a rate of Ca^{2+} increase consistent with that found in studies using Ca^{2+}

345   indicator dyes [12,18,19]. Thus, the MA104-GCaMP5G cells exhibit the well-characterized

346   hallmarks of RV-induced Ca^{2+} dysregulation but have greater spatial and temporal

347   resolution to study Ca^{2+} in RV-infected cells. This has revealed a new dimension of the

348   RV-induced Ca^{2+} signaling, in that the cytosolic Ca^{2+} increase manifests through highly

349   dynamic and discrete Ca^{2+} signaling events, which had not been previously observed.

350

351   **RV-induces dynamic Ca^{2+} signaling**

16

352   Our long-term Ca^{2+} imaging approach using MA104-GCaMP5G cells had

353 sufficient resolution to enable analysis of Ca^{2+} signaling at the single-cell level over the

354 course of the RV infection. Three representative traces from mock- or RV-infected cells

355 (MOI 10, imaged once per minute) show that while individual cells display unique

356 characteristics of Ca^{2+} signaling, they all exhibit similar patterns of Ca^{2+} signaling (Fig.

357 2A). Mock-infected cells maintain low cytosolic Ca^{2+} with few low amplitude Ca^{2+} signals

358 (Fig. 2A, black lines), but RV-infected cells display a large number of large amplitude

359 Ca^{2+} transients, as well as an overall increase in cytosolic Ca^{2+} (Fig. 2A, red lines).

360 These Ca^{2+} transients were the most prominent Ca^{2+} signal during the infection and

361 were infrequently detected in mock-infected cells. Finally, as RV is a lytic virus, we

362 observed clear evidence of cell lysis late in infection, but this was associated with a loss

363 of GCaMP5G signal and dynamics because the sensor diffused away from the ruptured

364 cells (see Supplementary Video 1 online). We sought to determine a threshold to define

365 these "Ca^{2+} spikes" so that we could measure the number and amplitude of these Ca^{2+}

366 signals. To define a "Ca^{2+} spike", we set a cutoff for the change in GCaMP5G

367 fluorescence between two measurements to be greater than 5% ($\Delta F > 5\%$). The mean

368 Ca^{2+} transient amplitude of mock-infected cells was 0.3% ($\pm$ 0.5% standard deviation)

369 (data not shown; see Fig. 2D for a subset of this data). Thus the $\Delta F > 5\%$ cutoff is more

370 than 3 standard deviations above the mean, which establishes a stringent threshold for

371 quantitating Ca^{2+} spikes. Next, we determined the change in fluorescence between

372 each data point and found that the majority of Ca^{2+} spikes were captured in 1 image

373 (Fig. 2B). This simple method enabled detection of Ca^{2+} spikes with approximately 80%

374 accuracy; however, it results in a 20% under-estimation of Ca^{2+} spikes, which were

17

375 captured in 2-3 images (Fig. 2C, black dots). Nevertheless, using this method of Ca^{2+}

376 spike analysis, we found that RV significantly increases the number of Ca^{2+} spikes per

377 cell (Fig. C). We then determined the amplitude for the top 150 Ca^{2+} spikes per

378 representative cell and found that while the amplitude was highly variable between RV-

379 infected cells, these signals were significantly greater than mock-inoculated cells (Fig.

380 2D). Finally, we compared the RV-induced Ca^{2+} spikes to the Ca^{2+} response induced by

381 10 μM ATP (Fig. 2E). As expected, ATP induced a strong Ca^{2+} flux that was similar to

382 the amplitude of Ca^{2+} spikes induced during RV infection. Although the ATP-induced

383 response was significantly greater than the RV-induced Ca^{2+} spikes, it is important to

384 note that the amplitude of the ATP-induced signals represent the peak of the Ca^{2+}

385 response, whereas it is not possible to know how many of the RV-induced Ca^{2+} spikes

386 were captured at the peak of the signal. Thus, at the individual cell level, a high MOI RV

387 infection induces up to hundreds of discrete and high amplitude Ca^{2+} signaling events.

388   Next, we determined how these RV-induced Ca^{2+} signals differ with respect to

389 different infectious doses. We infected MA104-GCaMP5G cells with SA114F or with a

390 recombinant SA11 cl. 3 expressing mRuby from the NSP3 gene (SA11cl3-mRuby) [28].

391 Cells were infected at MOI of 10, 1, or 0.1, and we performed time-lapse Ca^{2+} imaging

392 and single-cell analysis of the resulting Ca^{2+} signaling. Infection of cells with native

393 SA114F at different MOIs showed the expected infectious dose-dependent increase in

394 the number of RV-positive cells (Fig. 3A). Similarly, the SA11cl3-mRuby-infected cells

395 exhibited an infectious dose-dependent increase in the number of RFP-positive cells at

396 7 hpi (Fig. 3B), as well as an increase in RFP intensity from 7 hpi to 10 hpi (Fig. 3C).

397 Representative single-cell Ca^{2+} traces for SA114F-infected cells show similar dynamic

18

398   increases in cytosolic Ca^{2+} spikes as before, but cells infected with lower MOIs of 1 and

399   0.1 exhibited a later onset of the Ca^{2+} signaling and generally fewer and lower

400   amplitude Ca^{2+} spikes (Fig. 3D). The virus dose-dependent differences in the Ca^{2+}

401   signaling are clearly demonstrated by the time-lapse imaging at 6-7 hpi, which are

402   superimposed onto the immunofluorescence images to detect RV-positive cells

403   (Supplementary Video 2 online). In a more detailed examination of cytosolic Ca^{2+} in RV-

404   infected cells, we used a higher image acquisition frequency (1 image/1.5 sec) and

405   again observed active and dynamic Ca^{2+} signaling. While virtually every cell exhibited

406   multiple Ca^{2+} transients over the course of 10 mins, the Ca^{2+} spike frequency and

407   amplitude were variable from cell-to-cell (Supplemental Figure 1 & Supplementary

408   Video 3 online). We quantitated the number of Ca^{2+} spikes throughout the infection and

409   found a dose-dependent decrease in the number of spikes per cell (Fig. 3F) for lower

410   MOI infections. A similar phenotype was observed in cells infected with SA11cl3-

411   mRuby, but in this case the mRuby expression enabled us to measure both Ca^{2+}

412   signaling and RV protein expression (Fig. 3E & Supplementary Video 4 online). We

413   again observed that for lower MOI infections the onset of Ca^{2+} signaling was later, and

414   the Ca^{2+} spike number and amplitude were generally lower. Further, onset of the Ca^{2+}

415   signaling corresponded to the detection of mRuby from the NSP3 gene. Quantitation of

416   the number of Ca^{2+} spikes per cell for SA11cl3-mRuby infections also showed a dose-

417   dependent decrease with infectious dose (Fig. 3G). Thus, the number and amplitude of

418   these Ca^{2+} signaling events are related to both the infectious dose of RV and onset of

419   RV protein synthesis.

19

420   Next, we sought to characterize the Ca^{2+} signaling phenotype of different RV

421   strains that infect humans or other animals. We compared the Ca^{2+} signaling in MA104-

422   GCaMP5G cells infected at MOI 1 with simian strain SA114F to that of human strain Ito.

423   Immunofluorescence staining of Ito-infected cells (Fig. 4A) showed a similar number of

424   infected cells as that for SA114F infected above (Fig. 3A). As above, we quantitated the

425   number of Ca^{2+} spikes per cell and found that both SA114F and Ito induced a significant

426   increase in Ca^{2+} spikes compared to mock-infected cells (Fig. 4B). These findings

427   demonstrate that the dynamic Ca^{2+} signaling phenotype is not exclusively a feature of

428   animal RV strains. Further, we investigated the attenuated and virulent porcine OSU

429   strains (OSUa and OSUv). Mutations in the OSUa NSP4 protein are associated with

430   reduced elevation in cytosolic Ca^{2+} levels in recombinant NSP4-expressing Sf9 cells [40],

431   but the Ca^{2+} signaling phenotype of these two viruses had not been studied in the

432   context of an infection. Immunofluorescence of OSUa and OSUv-infected MA104 cells

433   at MOI 1 show a similar number of infected cells (Fig. 4A). However, while both OSUa

434   and OSUv significantly increase the number of Ca^{2+} spikes, the number of Ca^{2+} spikes

435   from OSUa-infected cells is significantly less than that of those infected with OSUv (Fig.

436   4B & Supplementary Video Movie 5 online). To characterize this difference further, we

437   examined single-cell traces for OSUa-and OSUv-infected cells (Fig. 4C). We found that

438   OSUa-infected cells initially induced a low-amplitude monophasic increase in cytosolic

439   Ca^{2+} levels (Fig. 4C, black arrows), with the onset of the dynamic Ca^{2+} spikes occurring

440   several hours later (Fig. 4C, purple traces). In contrast, OSUv infection induced a much

441   earlier onset of the dynamic Ca^{2+} spiking, which explains the higher number of Ca^{2+}

442   spikes per cell (Fig. 4C, blue traces). Interestingly, OSUv may also induce an early, low-

20

443   amplitude increase in cytosolic Ca^{2+} in addition to the dynamic Ca^{2+} spikes, but the high

444   number of Ca^{2+} spikes makes it difficult to clearly ascertain this in all but a few cells (Fig.

445   4C, red arrow). Together, these data demonstrate that the dynamic Ca^{2+} signaling

446   phenotype is a commonly feature among RV strains and potentially related to NSP4's

447   role in dysregulating host Ca^{2+} homeostasis and virus virulence.

448

449   **Ca^{2+} signaling dynamics are dependent on NSP4 expression**

450   RV NSP4 is the primary mediator of elevated Ca^{2+} levels during RV infection.

451   The differences in Ca^{2+} signaling by OSUa and OSUv observed in Fig. 4 suggest that

452   NSP4 expression is important for the induction of the dynamic Ca^{2+} signaling during

453   infection[1]. To test the role of NSP4 in these Ca^{2+} signals, we made two GCaMP6s cell

454   lines, each stably expressing a different short-hairpin RNA that targets SA11 NSP4

455   (NSP4 shRNA1 and NSP4 shRNA2), and a third GCaMP6s cell line stably expressing a

456   non-targeted scrambled shRNA. Cells were infected with SA114F (MOI 0.01), and we

457   found that cells expressing NSP4-targeted shRNAs exhibited knockdown of NSP4

458   protein levels (Fig. 5A). We normalized NSP4 expression to GAPDH and found ~40%

459   knockdown in cells expressing NSP4 shRNA1 and ~85% knockdown in cells expressing

460   NSP4 shRNA2 (Fig. 5B), which correlated with reduced RV plaque size (Fig. 5C). To

461   examine the Ca^{2+} signaling phenotype, we then infected the cells with SA114F (MOI

462   0.1) and used live-cell imaging to measure Ca^{2+} signaling from ~2-18 hpi. The

463   scrambled shRNA-expressing cells exhibited a similar degree of dynamic Ca^{2+} signaling

464   as observed in parental MA104 cells (Fig. 5D, red traces), whereas knockdown of NSP4

465   substantially decreased the degree of Ca^{2+} signaling observed (Fig. 5D, blue traces).

21

466   Upon quantitation, we found the number of Ca^{2+} spikes was significantly reduced in the

467   NSP4 knockdown cells (Fig. 5E). Together, these data show that NSP4 is responsible

468   for inducing these dynamic Ca^{2+} signals during infection.

469

470   **RV-induced Ca^{2+} spikes require extracellular and ER Ca^{2+} pools**

471   NSP4 elevates cytosolic Ca^{2+} by activating both uptake of extracellular Ca^{2+} and

472   release of ER Ca^{2+} pools. Thus, we next sought to characterize which pools of Ca^{2+}

473   were critical for supporting the RV-induced Ca^{2+} spikes. First, we tested whether

474   extracellular Ca^{2+} influenced the RV-induced Ca^{2+} spikes. We infected MA104-

475   GCaMP5G cells with SA114F (MOI 1), and at 1 HPI replaced the media with either

476   normal media containing 2 mM Ca^{2+}, media without Ca^{2+} (supplemented with 1.8 mM

477   EDTA), or media supplemented with Ca^{2+} for a 10 mM final concentration. The imaging

478   data shows that decreasing extracellular Ca^{2+} strongly reduced the number and

479   duration of Ca^{2+} signaling (Fig. 6A, light blue), whereas cells maintained in media with 2

480   mM or 10 mM extracellular Ca^{2+} showed increased dynamic Ca^{2+} signaling (Fig. 6A, red

481   & purple). As before, mock-infected cells in each condition exhibited little to no induction

482   of the Ca^{2+} signaling (Fig. 6A, black lines). Quantitation of the number of Ca^{2+} spikes

483   showed that RV-infected cells in low extracellular Ca^{2+} exhibited significantly fewer Ca^{2+}

484   spikes than that of cells in normal extracellular Ca^{2+}, but this was still greater than that

485   of mock-infected cells (Fig. 6B). Interestingly, there was no difference in the number of

486   Ca^{2+} spikes per cell when maintained in 2 mM versus 10 mM Ca^{2+} media (Fig. 6B).

487   However, the traces indicated that the magnitude of the Ca^{2+} spikes were greater in

488   high Ca^{2+} media. Thus, we then determined the Ca^{2+} spike amplitude for the top 50

22

489   Ca^{2+} spikes, and while this was highly variable from cell-to-cell, this trended to be

490   greater with higher extracellular Ca^{2+} concentrations (Fig. 6C). Together, these data

491   indicate that normal extracellular Ca^{2+} levels are critical for the RV-induced Ca^{2+} spikes,

492   which could occur both through discrete Ca^{2+} influx events through the plasma

493   membrane, and by influx of extracellular Ca^{2+} serving to maintain ER Ca^{2+} stores to

494   feed ER Ca^{2+} release events.

495   The ER is the major intracellular Ca^{2+} store, and RV NSP4 has been shown to

496   decrease ER Ca^{2+} levels both during infection and by recombinant expression [6,7].

497   However, controversy remains about whether RV causes a sustained depletion in ER

498   Ca^{2+} [22]. Thus to directly characterize the change in ER Ca^{2+} during RV infection, and

499   determine how this relates to the dynamic cytosolic Ca^{2+} spikes, we generated an

500   MA104 cell line co-expressing R-GECO1.2 and GCEPIAer (MA104-

501   RGECO1/GCEPIAer), in which R-GECO1.2 is a red fluorescent cytoplasmic GECI and

502   GCEPIAer is a green fluorescent ER-targeted GECI [24,41]. As above, infection with

503   SA114F (MOI 1) induced highly dynamic cytoplasmic Ca^{2+} signaling by ~8 hpi, as

504   illustrated in two representative single-cell traces (Fig. 7A-B, red traces; Supplementary

505   Video 6 online). Concomitant with the onset of the cytoplasmic Ca^{2+} signaling was an

506   equally dynamic decrease of ER Ca^{2+} that persisted throughout the rest of the infection

507   (Fig. 7A-B, green traces). We examined the relationship between the cytoplasmic Ca^{2+}

508   spikes and ER Ca^{2+} troughs more closely from 8-12 hpi (Fig. 7B), which was during the

509   onset of these signaling events. First, we found that the onset of Ca^{2+} signals in the

510   cytoplasm coincided with the ER Ca^{2+} release events (Fig. 7B, black arrowheads). The

511   persistent decrease in ER Ca^{2+} observed was driven primarily by this continuous

23

512 signaling, such that the ER Ca^{2+} level never recovered to the baseline level (Fig. 7A).

513 Interestingly, a small number of ER Ca^{2+} troughs were not associated with a

514 concomitant cytoplasmic Ca^{2+} spike (Fig. 7B, magenta arrowheads). Over the course of

515 the long-term imaging experiment, mock-infected cells exhibited a 10% decrease in

516 GCEPIAer fluorescence, but RV-infected cell had a 30% decrease (Fig. 7C), which

517 occurred rapidly from 8-12 HPI (Fig. 7A). The decrease in GCEPIAer in mock-infected

518 cells likely represents modest photobleaching of GCEPIAer over the imaging

519 experiment.

520   During these studies, we observed that the ER-localized GCEPIAer protein is

521 also redistributed during the RV infection, which is illustrated for a single cell in Fig. 7D-

522 E and Supplementary Video 7. At the beginning of the imaging run (3 hpi), the

523 GCEPIAer signal was high and localized throughout the ER in a reticular pattern (Fig.

524 7D-E, left) but by 10.7 HPI, RV-induced Ca^{2+} signaling had decreased GCEIPAer

525 fluorescence to its nadir (Fig. 7D-E, middle), representing a substantial decrease in ER

526 Ca^{2+}. Approximately 2 hrs after the initial decrease in ER Ca^{2+}, the GCEPIAer began

527 accumulating into circular domains that are likely the ER-derived compartment

528 surrounding viroplasms (Fig. 7D-E, right). These structures become more pronounced

529 through the late stages of the infection, ~13 hpi (Fig. 7D, arrows). While the absolute

530 onset of the ER Ca^{2+} release events was variable, the formation of viroplasm-

531 associated membranes subsequent to the decrease in ER Ca^{2+} was a consistent

532 pattern among RV-infected cells (Supplementary Video 7 online). Using immunostaining

533 and deconvolution microscopy, we confirmed that the structures are viroplasms

534 because they contain RV nonstructural protein 2 (NSP2), a major component of

24

535 viroplasms (Fig. 7F). Interestingly, during late stages of infection when viroplasms are

536 forming, we detected a modest recovery in ER Ca^{2+} from its nadir (Fig. 7E), which may

537 reflect the increased $^{45}Ca^{2+}$ uptake previously observed[22].

538

539 **SOCE blockers reduce RV-induced Ca^{2+} spikes**

540 Since removing extracellular Ca^{2+} diminishes the RV-induced Ca^{2+} spikes (Fig.

541 6), cellular Ca^{2+} influx pathways are critical for these Ca^{2+} signals. Several host Ca^{2+}

542 channels have been implicated in mediating Ca^{2+} entry into RV-infected cells, including

543 SOCE channels, voltage-activated Ca^{2+} channels (VACC), and the sodium-calcium

544 exchanger (NCX) [10-12]. To determine which pathway(s) were important for the dynamic

545 Ca^{2+} spikes in RV infection, we used pharmacological blockers targeting each pathway

546 (2-APB for SOCE; D600 for VACC; KB-R7943 for NCX). MA104-GCaMP5G cells were

547 infected with SA114F (MOI 1), and then treated with different concentrations of the

548 blockers at 1 hpi and imaged to measure GCaMP5G fluorescence. None of the blockers

549 exhibited cytotoxic effects to uninfected cells (data not shown). Cells treated with DMSO

550 as a vehicle control exhibited the dynamic Ca^{2+} spikes as above (Fig. 8A, red trace). In

551 contrast, cells treated with the SOCE blocker 2-APB exhibited a dose-dependent

552 decrease in both the number and amplitude of the Ca^{2+} signaling (Fig. 8A, green

553 traces). Traces from cells treated with the NCX blocker KB-R7943 showed a modest

554 decrease in Ca^{2+} signaling (Fig. 8A, brown traces), whereas there was no difference in

555 Ca^{2+} signaling for cells treated with D600 (data not shown). We also noted that RV-

556 infected cells treated with 10 µM KB-R7943 underwent cell death more frequently than

557 any other treatment, which was marked by a rapid increase in cytosolic Ca^{2+} and then

25

558   lysis (Fig. 8A, arrowhead); however, cell death was not observed in uninfected cells

559   treated with KB-R7943 (data not shown). We quantitated the number of Ca^{2+} spikes per

560   cell, which showed a significant, dose-dependent decrease in the number of Ca^{2+}

561   spikes for both 2-APB-treated (Fig. 8B, green) and, to a lesser extent, KB-R7943-

562   treated (Fig. 8B, brown) cells, but no difference for D600-treated cells (Fig. 8B, blue).

563   We further investigated the effects of 2-APB and KB-R7934 by examining the amplitude

564   of the largest 50 Ca^{2+} spikes of three representative cells shown in Fig. 8C-D.

565   Treatment with 2-APB showed a dose-dependent decrease in the Ca^{2+} spike amplitude

566   (Fig. 8C), consistent with the single-cell traces, but treatment with KB-R7943 showed no

567   difference in spike amplitude.

568   Since elevated cytosolic Ca^{2+} is critical for RV replication, we examined RV

569   protein levels by immunoblot to determine whether 2-APB or KB-R7943 reduced the

570   Ca^{2+} signaling by merely blocking RV or NSP4 protein synthesis or protein stability[42].

571   Immunoblot detection with an anti-RV antisera (Fig. 8E) or an anti-NSP4 specific

572   antisera (Fig. 8F) show that none of the Ca^{2+} channel blockers caused substantial

573   decrease in RV or NSP4 protein levels. However, we observed that 2-APB treatment

574   significantly increased the 20 kDa unglycosylated NSP4 band (Fig. 8F) by gel

575   densitometry analysis (Fig. 8G).

576   Overall the SOCE blocker 2-APB was the most potent inhibitor of the RV-induced

577   dynamic Ca^{2+} signaling, so we examined the effect of other SOCE blockers that also

578   target the Orai1 Ca^{2+} channel. MA104 cells express the Orai1 Ca^{2+} channel and the

579   STIM1 and STIM2 ER Ca^{2+} sensors, which are the core machinery for the SOCE

580   pathway (Fig. 9A). While MA104 cells also express the Orai3 Ca^{2+} channel, this isoform

26

581   is not activated by ER Ca^{2+} store depletion but arachidonic acid and leukotrienes [43]. We

582   tested four SOCE blockers (2-APB, BTP2, Synta66, and GSK7975A) for the ability to

583   block thapsigargin-induced SOCE and found that all of them showed a similar inhibition

584   of Ca^{2+} entry after ER store depletion (Fig. 9B). Thus, we treated SA114F-infected

585   MA104-GCaMP5G cells with each of these blockers at ~1hpi and performed Ca^{2+}

586   imaging to measure the RV-induced Ca^{2+} spikes (Fig. 9C-D). Representative single-cell

587   traces illustrate that all the SOCE blockers inhibited the RV-induced dynamic Ca^{2+}

588   signaling (Fig. 9C) and significantly inhibited the number of Ca^{2+} spikes per cell (Fig.

589   9D). The blockers displayed varying degrees of potency but 2-APB and BTP2 treatment

590   caused the greatest decrease in RV-induced Ca^{2+} signaling (Supplementary Video 8

591   online). Further, we found that treatment with the SOCE blockers significantly reduced

592   RV yield from MA104 cells (Fig. 9E), which is consistent with the importance of elevated

593   cytosolic Ca^{2+} for RV replication[29]. As with the other Ca^{2+} channel blockers, we

594   examined whether the SOCE blockers affected viral protein levels by immunoblot. As

595   above, we found that 2-APB treatment increased the abundance of the 20 kDa

596   unglycosylated NSP4 band (NSP4-20), and Synta66 treatment also caused a modest

597   increase in NSP4-20 (Fig. 9F). In contrast to the other SOCE blockers, BPT2 treatment

598   caused an overall decrease in RV proteins, which correlates with the strong

599   suppression of RV-induced Ca^{2+} signaling during the infection (Fig. 9D & 9F). Together,

600   these data support the previous observation that shRNA knockdown of the Ca^{2+} sensor

601   STIM1 reduces RV replication, and further show that Ca^{2+} influx *via* SOCE channels is

602   critical for RV-induced Ca^{2+} signaling and replication[10].

603

27

Human intestinal enteroid characterization of RV-induced Ca^{2+} signaling

Although MA104 cells provide a robust model for RV replication and form a single epithelial sheet ideal for microscopy studies, they are neither of human nor of intestinal cell origin. Human intestinal enteroids (HIEs) have been developed as a model *in vitro* system of the epithelial cells of the small intestine, and support RV infection and replication, particularly for human RV strains [26,44]. HIEs are grown in "mini-gut" three-dimensional (3D) cultures from human intestinal stem cells and are non-transformed cells, which make them a biologically relevant system to study the GI epithelium[45]. Thus, we sought to determine if the dynamic cytosolic Ca^{2+} signaling observed in MA104 cells were also observed in HIEs with RV infection.

We created jejunum HIEs stably expressing the green cytoplasmic GECI GCaMP6s (jHIE-GCaMP6s) using lentivirus transduction. To test the response of GCaMP6s to cytoplasmic Ca^{2+} in the enteroids, we treated 3D jHIE-GCaMP6s stabilized in a diluted Matrigel, with carbachol, a known Ca^{2+} agonist. Carbachol treatment of jHIE-GCaMP6s significantly increased GCaMP6s fluorescence 200-300% over the mock-treated jHIE-GCaMP6s (Fig. 10A-C). Thus, jHIE-GCaMP6s enteroids functionally report changes in cytoplasmic Ca^{2+} and can be used to examine RV-induced Ca^{2+} signaling.

We next tested if 3D jHIE-GCaMP6s enteroids would exhibit similar Ca^{2+} dynamics during RV infection as observed in MA104-GCaMP5G cells. jHIE-GCaMP6s enteroids were mock- or RV-infected with the human RV strain Ito, seeded into chamber slides in diluted Matrigel, and imaged every 2-3 minutes for phase contrast and GCaMP6s fluorescence throughout the RV infection (~16 hrs). At 24 hpi, the HIEs were fixed and immunostained for RV antigens to confirm successful infection, which is

28

627   evident by both infected cells within the HIEs as well as strong positive staining of the

628   dead cells sloughed from the HIEs (Fig. 10D). Examination of the Ca^{2+} signaling

629   showed little Ca^{2+} signaling activity in the mock-infected jHIE-GCaMP6s enteroids, but

630   RV-infected enteroids exhibited significantly increased Ca^{2+} dynamics, as illustrated in

631   representative traces from three mock- or RV-infected HIEs (Fig. 10E and

632   Supplementary Video 9 online). Similar to the Ca^{2+} signaling observed in MA104 cells,

633   initially there were no or only modest changes in cytosolic Ca^{2+}, and the onset of strong

634   and dynamic Ca^{2+} signals occurred ~8-10 HPI. For HIEs it was not possible to

635   accurately measure Ca^{2+} signaling at the single-cell level. We were able to track and

636   measure Ca^{2+} signaling over the entire jHIE-GCaMP6s enteroid and quantify these

637   changes as Ca^{2+} spikes/enteroid. We found that RV significantly increased the number

638   of Ca^{2+} spikes/enteroid (Fig. 10F) and that the Ca^{2+} spike amplitudes are also

639   substantially greater in RV-infected than in mock-infected jHIE-GCaMP6s enteroids

640   (Fig. 10G). Thus, the RV-induced Ca^{2+} signaling in enteroids closely parallels that

641   observed in MA104 cells and demonstrate that these dynamic Ca^{2+} signals are a

642   biologically relevant aspect of how RV disrupts host Ca^{2+} homeostasis.

643   Since SOCE played a prominent role in the RV-induced dynamic Ca^{2+} signaling

644   in MA104 cells, we investigated whether it was also critical for the Ca^{2+} signaling

645   observed in HIEs. Similar to MA104 cells, jejunum-derived HIEs expressed the core

646   SOCE proteins Orai1, STIM1, and STIM2, as well as the non-store operated Orai3

647   channel (Fig. 11A). The expression levels were not substantially altered by

648   differentiating the jHIEs through removal of growth factors. To test whether SOCE is

649   important for RV-induced Ca^{2+} signaling, we first tested 2-APB treatment of 3D jHIE-

29

650   GCaMP6s enteroids either mock- or RV-infected with strain Ito. While RV infection

651   increased the number of Ca^{2+} spikes per enteroid consistent with above (Fig. 11B), 2-

652   APB treatment did not attenuate the Ca^{2+} signaling (Fig.11B-C). We speculated that the

653   3D format or the Matrigel used to support 3D HIEs might interfere with 2-APB blocking

654   SOCE, so we repeated these studies using jHIE-GCaMP6s monolayers. First, we

655   confirmed that 2-APB can block thapsigargin-induced SOCE in jHIE-GCaMP6s

656   monolayers, which exhibited a 32% reduction in Ca^{2+} re-entry after store depletion (Fig.

657   11D). Interestingly, 2-APB shows a much less potent block of SOCE in enteroids than in

658   MA104 cells, which exhibited a >80% inhibition of Ca^{2+} re-entry after store depletion

659   (Fig. 9C). We also tested if VACC or NCX may contribute to RV-induced Ca^{2+} signaling

660   in enteroids, but treatment with D600 or KB-R7943 did not reduce Ca^{2+} spikes in RV-

661   infected jHIE-GCaMP6s monolayers (Fig. 11E). Nevertheless, 2-APB treatment of both

662   mock-inoculated (Fig. 11F, black vs. grey traces) and RV-infected jHIE-GCaMP6s

663   monolayers (Fig. 11F, red vs. blue traces) reduced the observed Ca^{2+} signaling, as

664   illustrated in the representative traces (see Supplementary Video 10 online). We

665   quantitated the Ca^{2+} signaling per FOV and confirmed that 2-APB treatment significantly

666   reduced the number of Ca^{2+} spikes for both mock and RV-infected enteroids (Fig. 11G),

667   as well as substantially reducing the amplitude of the Ca^{2+} signals (Fig. 11H). Thus, like

668   the MA104 model, SOCE is critical for supporting the dynamic Ca^{2+} signaling induced in

669   RV-infected jHIEs.

Discussion

A hallmark of RV infection, and several other viruses, is an elevation in cytosolic Ca^{2+} and decrease in ER Ca^{2+} stores, which facilitates virus replication and contributes to pathogenesis through a variety of downstream pathways [1,46]. The importance of RV-induced dysregulation of Ca^{2+} levels for many of these downstream pathways has been determined, but thus far characteristics of the Ca^{2+} signaling itself have not been extensively investigated [1,5]. Thus, the primary goal of this study was to determine the nature of the RV-induced elevation in cytosolic Ca^{2+} and characterize how the dysregulation of Ca^{2+} signaling manifests during the infection. By leveraging GECI-expressing cell lines to perform long-term Ca^{2+} imaging, we found that RV induces a vast increase in Ca^{2+} signaling events that increased in frequency and magnitude over the course of the infection. These results are consistent with previous measurements of cytosolic Ca^{2+} in RV-infected cells that show a monophasic increase over time, which is similar to our imaging data when it is averaged out across the whole FOV (*i.e.*, a cell population). Yet, what is paradigm changing is that at the individual cell level, RV does not merely cause a steady increase in cytosolic Ca^{2+}, but rather activates a cacophony of discrete Ca^{2+} signaling events. Further, by generating GECI-expressing HIEs, this study is the first characterization of RV-mediated Ca^{2+} signaling in normal, human small intestinal enterocytes. We found that the prominence of the Ca^{2+} spikes in RV-infected HIEs is similar to that in MA104 cells, underlining that this is a biologically relevant phenomenon.

The characterization of the RV-induced increase in cytosolic Ca^{2+} as a series of discrete, transient Ca^{2+} signals is an important new insight into the cellular

31

693   pathophysiology of RV infection. Transient increases in cytosolic Ca^{2+} serve as pro-

694   survival signals by activating phosphoinositide 3-kinase (PI3K) and by calcineurin-

695   dependent NFAT activation. Further, Ca^{2+} oscillations stimulate mitochondrial Ca^{2+}

696   uptake that enhances ATP synthesis, and this increase in mitochondrial metabolism

697   contributes to cell survival pathways. In contrast, strong sustained elevation of cytosolic

698   Ca^{2+} drives pro-apoptotic signaling through mitochondrial Ca^{2+} overload[20]. Thus, even

699   though the mean cytosolic Ca^{2+} level is progressively increasing in the RV-infected cell,

700   early activation of the intrinsic apoptotic cascade may be prevented because it occurs

701   as hundreds of transient Ca^{2+} signals over hours. This premise is consistent with

702   studies showing that early activation of PI3K during RV infection delays apoptosis[47].

703   Concomitantly, the elevated Ca^{2+} signaling activates cellular pathways, such as

704   autophagy, that promote RV replication and assembly of progeny virus[29]. Whether the

705   initial Ca^{2+} dynamics enhance mitochondria bioenergetics or ATP synthesis early during

706   RV infection has not been studied, but a loss of mitochondria membrane potential and

707   decrease in ATP output occur at late stages of infection[47,48]. Ultimately the massive

708   increase in Ca^{2+} signaling damages the cell and triggers cell death, and cell lysis was

709   observed in our time-lapse imaging, but this data cannot differentiate whether this was

710   through apoptosis, necrosis, and/or pyroptosis[18,47,49]. Thus, RV exploitation of discrete

711   Ca^{2+} signals, rather than a sustained increase in cytosolic Ca^{2+}, may function in concert

712   with other RV anti-apoptotic proteins, such as NSP1, to forestall the onset of cell death

713   and enable sustained viral replication.

714   Due to GECI photostability, we were, for the first time, able to perform Ca^{2+}

715   imaging of individual cells throughout the RV infection. The increased Ca^{2+} spikes are

716   the predominant feature of this imaging, and the SA11-mRuby reporter virus

717   demonstrates that the onset of the increased Ca^{2+} signaling correlates with RV protein

718   synthesis as well as input virus dose. Yet, despite individual cells exhibiting very distinct

719   Ca^{2+} signaling traces, a general pattern emerges: [i] early in infection Ca^{2+} signaling

720   remains at basal levels; [ii] onset of increased Ca^{2+} signaling is characterized by low-

721   amplitude Ca^{2+} spikes relatively; and then [iii] very high-amplitude Ca^{2+} spikes become

722   predominant, which results in elevated cytosolic Ca^{2+} levels. The progression of the RV-

723   induced Ca^{2+} signals have important implications for characterizing how Ca^{2+}-regulated

724   cellular processes are influenced by RV infection. For example, RV induces autophagy

725   through increased cytosolic Ca^{2+}, thereby activating calcium/calmodulin-dependent

726   kinase kinase-β (CaMKKβ)[29]. This raises several questions: *When* after onset of the

727   aberrant Ca^{2+} signaling is CaMKKβ activated? *How many* Ca^{2+} signals are needed to

728   induce autophagy? Similar questions can be asked about the role of these Ca^{2+} signals

729   in RV-induced apoptosis, cytoskeletal rearrangement, and serotonin and chloride

730   secretion[26,47,50,51]. Tracking these dynamic relationships poses a challenge that may be

731   addressed by further engineering GECI-expressing cell lines/HIEs to express other

732   biosensors such that both processes can be measured throughout the infection.

733   Many studies show that RV infection (or NSP4 expression) reduces the ER Ca^{2+}

734   stores based on a blunted cytosolic Ca^{2+} release in response to agonists (*e.g.*, ATP) or

735   thapsigargin treatment to prevent SERCA-mediated refilling[22,52]. However, other results

736   show increased in radioactive $^{45}Ca^{2+}$ loading into the ER in RV-infected cells, which is

737   hypothesized to be due to an increase in Ca^{2+} binding proteins (*e.g.*, VP7 or ER

738   chaperone proteins)[7,11]. Thus, controversy remains about whether RV causes a

739 decrease in the ER Ca^{2+} store. To address this question, we developed MA104-

740 RGECO1.2/GCEPIAer cells to directly measure cytosolic and ER Ca^{2+} together during

741 the RV infection. RV induces a dynamic decrease in ER Ca^{2+} levels that occurs in

742 conjunction with the increase in cytosolic Ca^{2+} signaling. In most instances, the cytosolic

743 Ca^{2+} spike correlated with a decrease in ER Ca^{2+}, indicating release of ER Ca^{2+}

744 substantially contributes to the increased cytosolic Ca^{2+} signaling. Further, despite the

745 30% reduction in steady-state ER Ca^{2+}, the dynamic nature of the ER Ca^{2+} signaling

746 suggests that SERCA pumps continually work to refill the ER. The observed depletion

747 of ER Ca^{2+} levels is consistent with the blunted cytosolic response to Ca^{2+} agonists like

748 ATP, the NSP4 function as a Ca^{2+}-conducting viroporin in the ER, and the activation of

749 the ER Ca^{2+} sensor STIM1[7,9,10]. In contrast, it is more difficult to reconcile the previously

750 observed increase in $^{45}Ca^{2+}$ loading into the ER with the 30% reduction in steady-state

751 ER Ca^{2+} levels detected by GCEPIAer imaging in this study. It has been hypothesized

752 that increased $^{45}Ca^{2+}$ loading may be due to increased ER Ca^{2+} buffering capacity,

753 caused by the high levels of RV VP7 and/or chaperones BiP and endoplasmin[11].

754 However, our data suggest this is unlikely to be the case because this would sequester

755 Ca^{2+} and render GCEPIAer unresponsive to changes in ER Ca^{2+}[24], yet this is not the

756 case because GCEPIAer remains dynamic throughout the infection. Alternatively, the

757 increase $^{45}Ca^{2+}$ may reflect loading into the ER-derived autophagy-like microdomains

758 that surround viroplasms, which we observed form after the initial depletion in ER Ca^{2+}

759 and during a partial recovery of ER stores[29,53]. These ER microdomains are the site

760 VP7 assembly onto nascent RV particles, which requires high Ca^{2+}, so Ca^{2+}

761 sequestration in these microdomains may occur independently of the rest of the ER.

34

762 Future studies using GCEPIAer and viroplasm-targeted GECIs are needed to determine

763 whether the ER and viroplasm-associated membranes are functionally distinct

764 compartments.

765   The pleiotropic functions of NSP4 are responsible for the RV-mediated

766 dysregulation of host Ca^{2+} homeostasis through the ion channel function of iNSP4 and

767 Ca^{2+} agonist function of the secreted eNSP4 enterotoxin [5,9,10]. Our data show that NSP4

768 governs the dynamic Ca^{2+} signaling induced by RV infection since NSP4 knockdown

769 significantly abrogated the number and amplitude of the Ca^{2+} spikes. Unfortunately, it is

770 not possible to determine the relative roles of iNSP4 versus eNSP4 in the induction of

771 the Ca^{2+} spikes from these data because the shRNA decreased total NSP4 synthesis,

772 and therefore both pathways would be attenuated. The importance of NSP4 for the Ca^{2+}

773 signaling is also demonstrated by the extremely different Ca^{2+} signaling profiles of

774 OSUa- and OSUv-infected cells. These differences correlate with the attenuated

775 elevation of cytosolic Ca^{2+} caused by recombinant OSUa NSP4 both when expressed in

776 Sf9 cells (*i.e.*, iNSP4) and exogenous treatment of cells (*i.e.*, eNSP4)[40]. The attenuated

777 NSP4 phenotype is the result of mutations in the NSP4 enterotoxin domain, indicating

778 that this domain is critical for induction of the Ca^{2+} spikes by OSU[25,40]. However, it is

779 important to note that these two viruses are not isogenic so the genetic backgrounds of

780 the OSUa and OSUv NSP4 are different, requiring further Ca^{2+} imaging studies using

781 recombinant RV bearing these attenuating NSP4 mutations to fully dissect the relative

782 importance iNSP4- and eNSP4-mediated Ca^{2+} signaling.

783   NSP4 is the trigger of the dynamic Ca^{2+} signaling, yet these signals are

784 maintained through host Ca^{2+} channels and signaling pathways both in the ER and PM.

35

785   Removal of extracellular Ca^{2+} significantly attenuated the Ca^{2+} spikes, demonstrating

786   that Ca^{2+} influx is crucial for these signals. Three classes of Ca^{2+} channels (SOCE,

787   NCX, and VACC) have been implicated RV-induced Ca^{2+} influx[10-12,23]. Our results using

788   different pharmacological blockers indicate SOCE is the primary Ca^{2+} influx pathway

789   that supports the RV-induced dynamic Ca^{2+} spikes, both in MA104 cells and in HIEs.

790   Blocking SOCE significantly reduced the number and amplitude of the RV-induced Ca^{2+}

791   spikes. However, the Orai1 SOCE channel is a very low conductance channel so Ca^{2+}

792   entry through PM Orai1 is unlikely to generate the high amplitude Ca^{2+} spikes observed

793   during RV infection. The nature of the Ca^{2+} spikes, and the fact that most of them

794   coincide with ER Ca^{2+} troughs, indicates that the signals detected are ER Ca^{2+}-release

795   events. ER Ca^{2+} release could occur either through iNSP4 or activation of the IP_3-

796   Receptor Ca^{2+} channel, and SOCE serves to maintain these signals by sustaining ER

797   Ca^{2+} refilling. Since elevated Ca^{2+} levels are critical for RV replication, the attenuated

798   Ca^{2+} signaling caused by the SOCE blockers significantly reduced RV yield[29].

799   Interestingly, blocking SOCE in HIEs significantly reduced the Ca^{2+} spikes, but the

800   effect was less pronounced than in MA104 cells, suggesting other pathway(s) may exist

801   that support RV-induced Ca^{2+} spikes in HIEs.

802   In summary, RV dysregulates host Ca^{2+} homeostasis by a massive and

803   progressive increase in discrete Ca^{2+} signaling events, mainly from ER Ca^{2+} release.

804   Many viruses elevate cytosolic Ca^{2+} and alter ER Ca^{2+}, leading us to question whether

805   dynamic Ca^{2+} spikes, as seen in RV infection, is a common manifestation for virus-

806   induced Ca^{2+} signaling. If so, the host channels that support these Ca^{2+} signals, such as

36

807   Orai1, may represent novel targets for broadly acting host-directed antiviral

808   therapeutics.

826

827   **Author Contributions.** JH, ACG, JP, AS, JC and MKE designed the experiments and

828   discussed the data. JH, ACG, JP, NR, and AS conducted the calcium imaging experiments and

829   analyzed the data with JH and ACG. JC and MKE provided key reagents including the shRNA

830   knockdown cells. JP conducted the western blot and plaque assays and analyzed data with JH.

831   AS and ACG conducted and analyzed qPCR experiments. JH and ACG wrote the manuscript,

832   and all authors contributed to revisions of the paper.

833
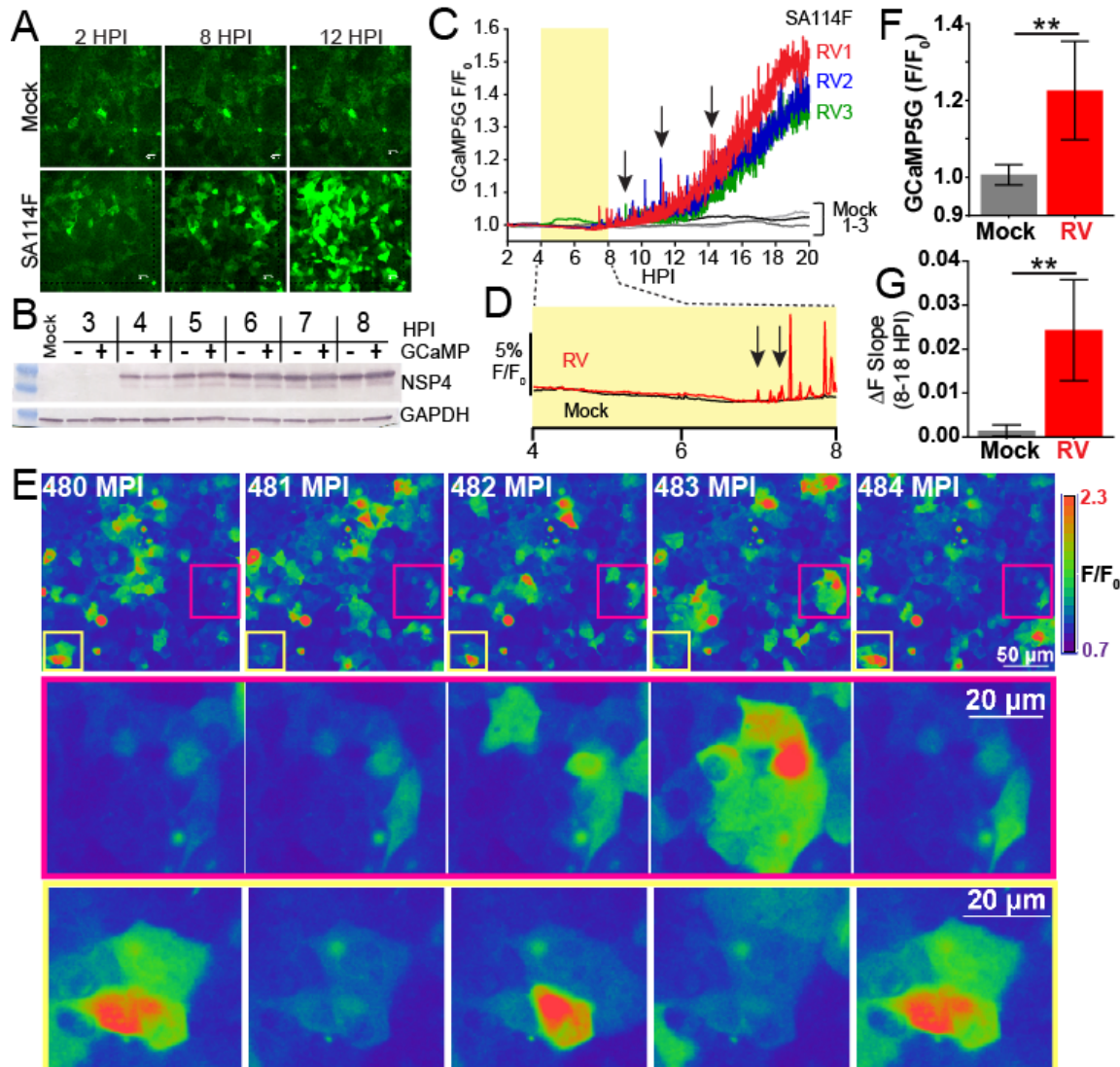
Figures

Figure 1. RV-induced increase in cytosolic Ca^{2+} manifests as increased Ca^{2+} signaling dynamics. (A) Epifluorescence images of mock (upper) or SA114F-infected (MOI 10) MA104-GCaMP5G cells at 2, 8, and 12 hours post-infection (HPI). **(B)** Western blot of RV NSP4 expression in MA104 cells without (-) or with (+) GCaMP5G from 3-8 HPI. Western blot for GAPDH serves as a loading control. **(C)** GCaMP5G fluorescence (F/F$_0$) for three fields-of-view (~455 μm^2) each of mock (black and grey lines) or RV-infected (red, blue, and green) MA104-GCaMP5G cells from 2-20 HPI. Increased frequency of transient Ca^{2+} fluxes (arrows) highlight the increased Ca^{2+} signaling dynamics. **(D)** Expanded graph of relative GCaMP5G (F/F$_0$) of representative Mock (black) and RV-infected (red) cells. Arrows indicate the increased low/moderate amplitude Ca^{2+} signals present during the initial increase in steady-state cytosolic Ca^{2+}. **(E)** Examples of the dynamic Ca^{2+} signaling. GCaMP5G fluorescence pseudocolored by intensity from 480-484 minutes post-infection (MPI). Regions in the magenta and yellow boxes are magnified below. **(F)** Average GCaMP5G fluorescence from 18-19 HPI and **(G)** slope of GCaMP5G ΔF from 8-18 HPI. Data shown as mean ± SD from 12 fields-of-view (triplicate of four independent experiments). **p<0.01

39

851

852
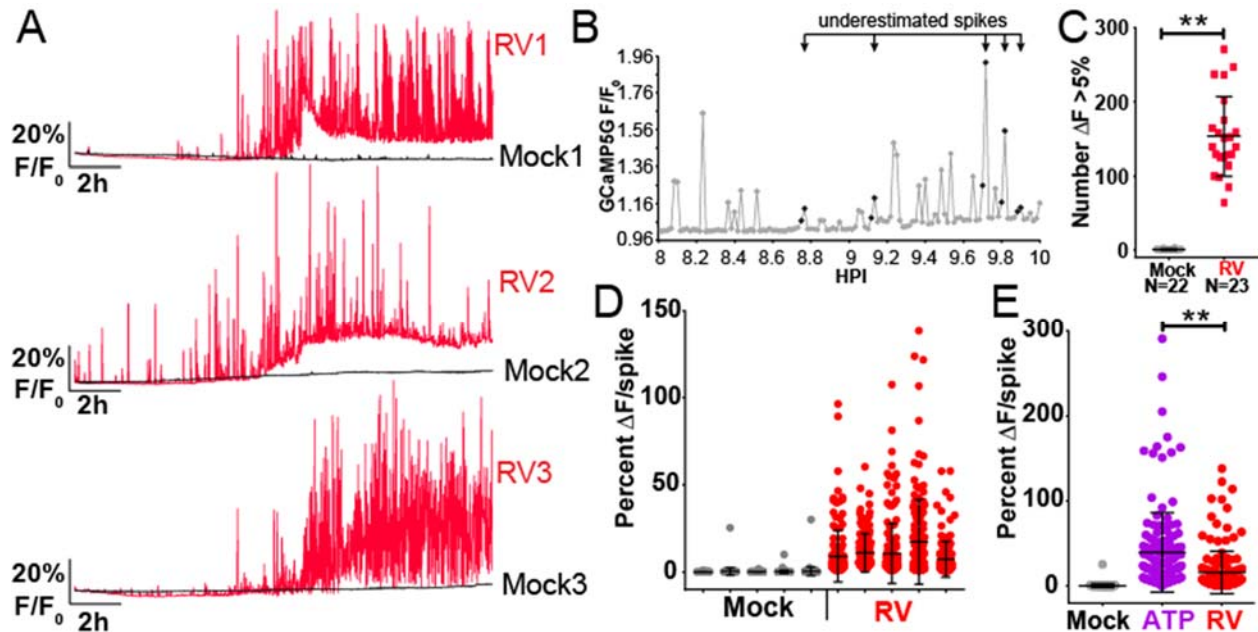
853 **Figure 2. RV increases the number and amplitude of Ca^{2+} spikes at the single-cell level.**
854 **(A)** GCaMP5G (F/F$_0$) fluorescence traces from three representative single mock (black) or RV-
855 infected (red) MA104-GCaMP5G cells. **(B)** GCaMP5G fluorescence (F/F$_0$) of a single RV-
856 infected MA104-GCaMP5G cell from 8-10 HPI. Symbols in magenta denote Ca^{2+} spikes
857 captured in two data points and potentially underestimated by counting spikes as ΔF >5%. **(C)**
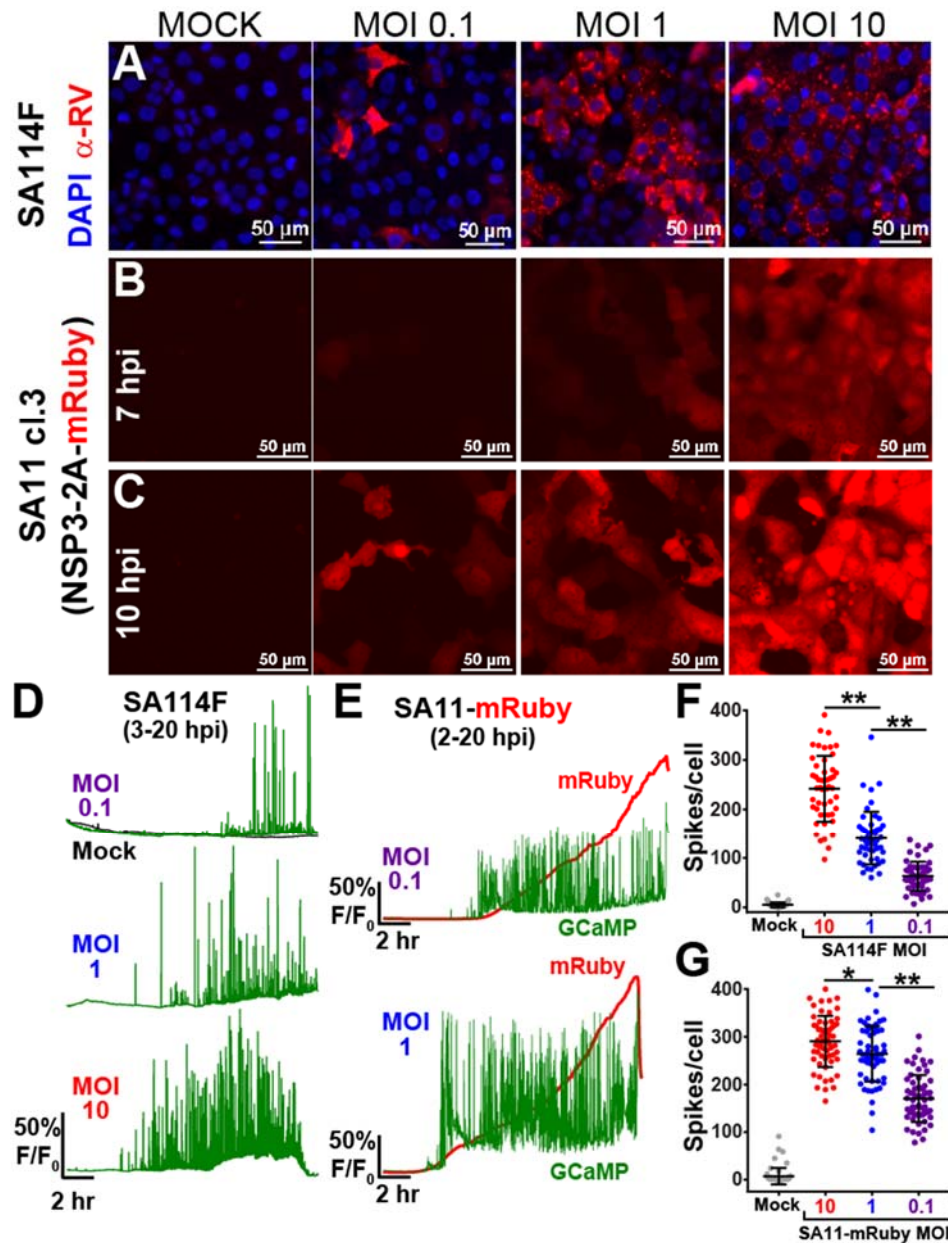858 MA104-GCaMP5G cells mock or RV infected (MOI 10), GCaMP5G fluorescence was imaged
859 from 2-20 HPI and the number of Ca^{2+} spikes (ΔF >5%) individual cells was determined. **(D)**
860 Ca^{2+} spike amplitude of the top 150 Ca^{2+} spikes from five representative mock and RV-infected
861 cells. **(E)** GCaMP5G Ca^{2+}response to 50 µM ATP in comparison to mock or RV infection. Data
862 shown as mean ± SD. **p<0.01

863

Figure 3. RV-induced dynamic Ca²⁺ signaling is related to virus dose. (A) Immunofluorescence images of mock or SA114F-infected MA104-GCaMP5G cells that were inoculated with increasing MOI (0.1, 1, or 10). RV antigen (red) is detected at ~8 hpi with anti-RV polyclonal antisera and nuclei are stained with DAPI (blue). **(B-C)** Epifluorescence images of MA104-GCaMP5G cells mock or infected with recombinant SA11-mRuby reporter virus with increasing MOIs (0.1, 1, 10). Images were captured at 7 HPI **(B)** or 10 HPI **(C)**. **(D)** Representative single-cell traces of relative GCaMP5G fluorescence (F/F_0) from cells mock (black) or RV infected by SA114F with MOIs of 0.1 (purple), 1 (blue), 10 (red). **(E)** Representative single-cell traces of relative fluorescence (F/F_0) of GCaMP5G (green) and mRuby (red) from cells infected by SA11-mRuby MOI 0.1 (purple) or 1 (blue). **(F-G)** Number of Ca²⁺ spikes ($F/F_0 > 5\%$) from mock or RV-infected cells that were infected with SA114F **(F)** or SA11-mRuby **(G)**. Data shown as mean $\pm$ SD of 60 cells/condition. **p<0.01

41

879
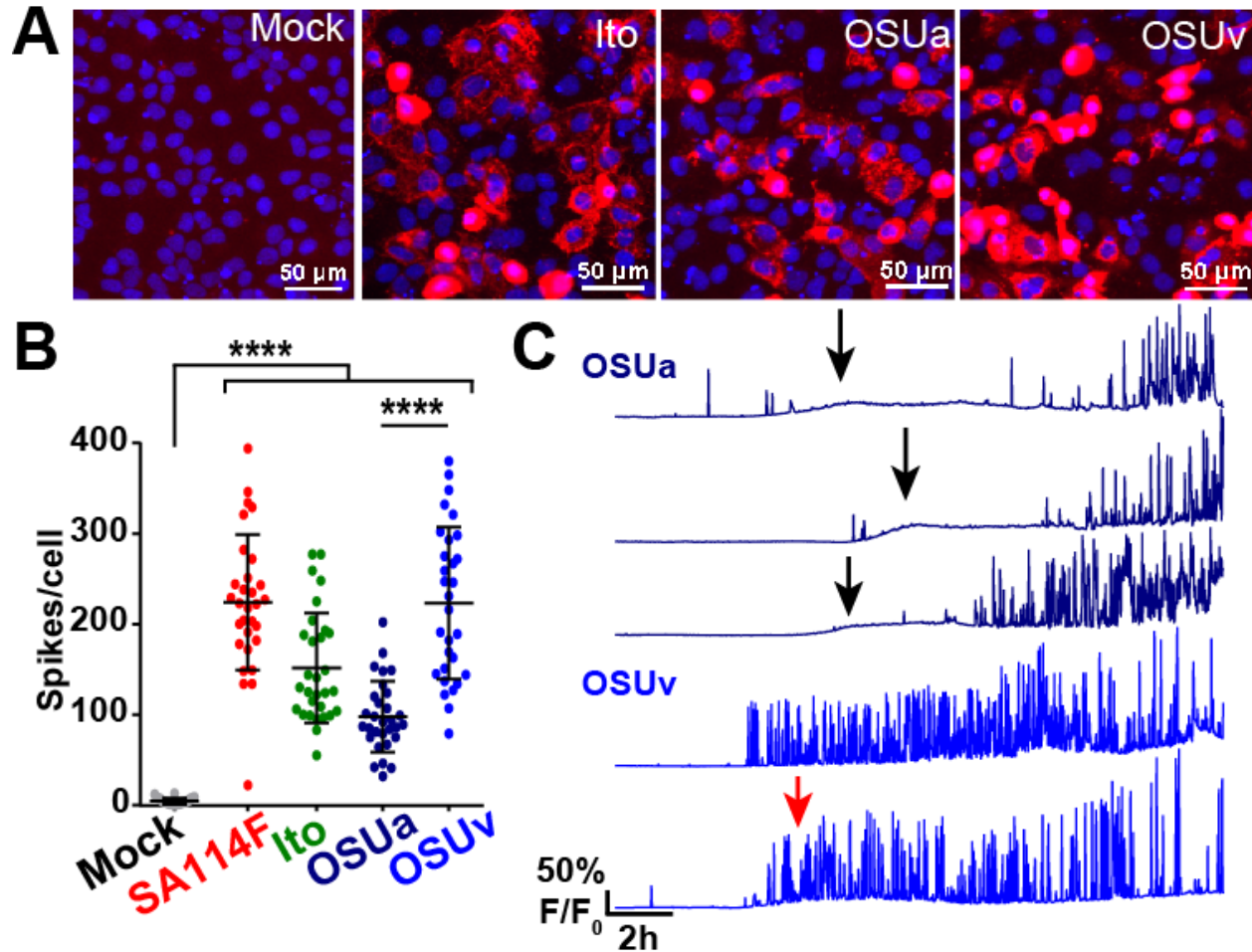
Figure 4. Dynamic Ca^{2+} signaling is induced by several other RV strains. (A)
Immunofluorescence images of MA104-GCaMP5G cells mock or infected by human RV strain
Ito, porcine OSUa, or porcine OSUv at MOI 1. RV antigen (red) is detected at ~8 hpi with anti-
RV polyclonal antisera and nuclei are stained with DAPI (blue). **(B)** Number of Ca^{2+} spikes (F/F$_0$
> 5%) from mock or RV-infected cells inoculated with MOI1 of the strains listed. Data shown as
mean $\pm$ SD of 30 cells/condition. ****p<0.0001. **(C)** Representative single-cell traces of relative
GCaMP5G fluorescence (F/F$_0$) from cells infected by OSUa (purple) or OSUv (blue). A slight
increase in the steady-state Ca^{2+} level is exhibited by most OSUa-infected (black arrows) and
some OSUv-infected (red arrow) cells.

889

42
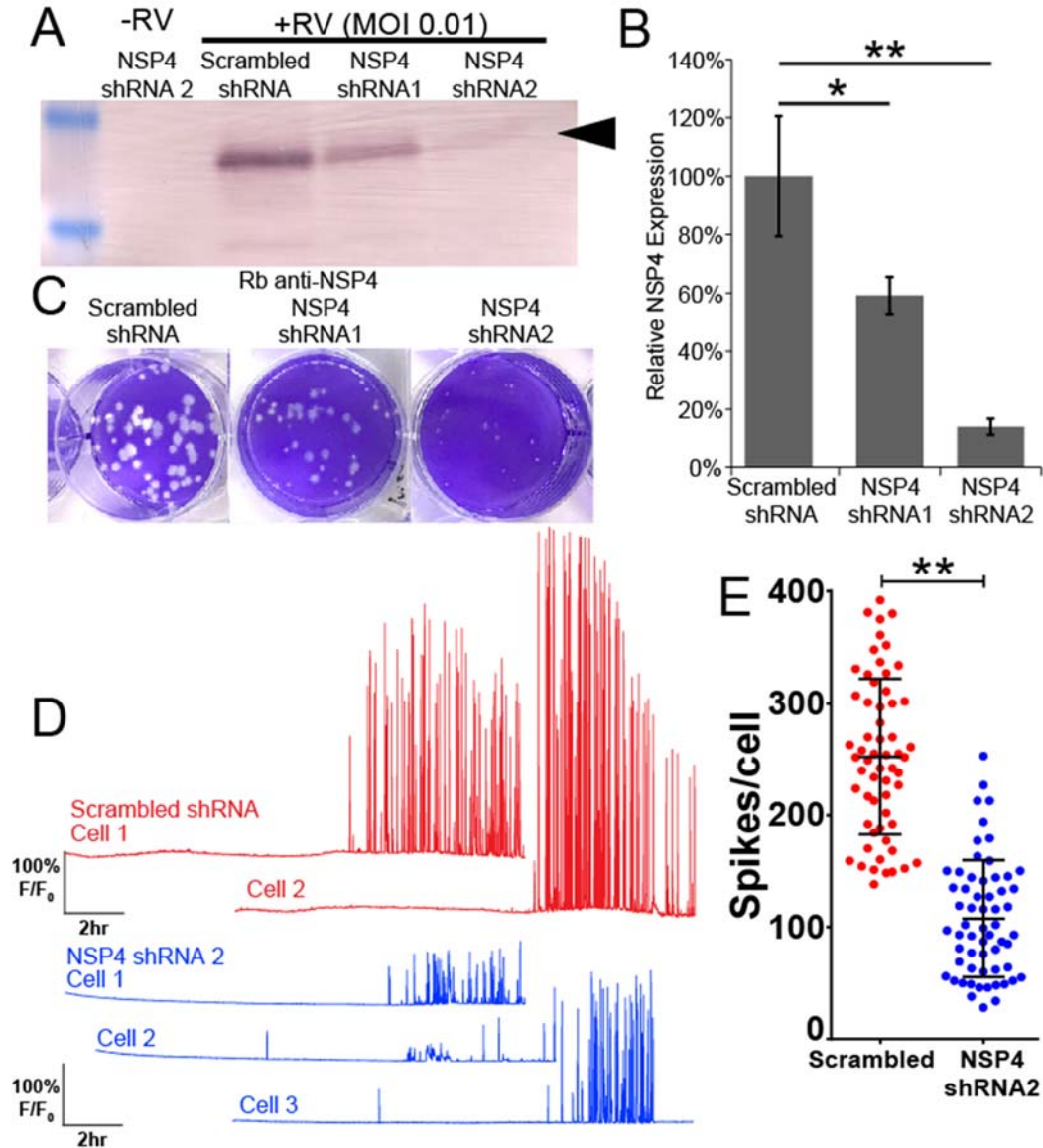
Figure 5. Knockdown of NSP4 reduces the dynamic Ca^{2+} signaling. (A) Western blot for NSP4 expression in mock infected or RV-infected MA104-GCaMP6s/shRNA cell lines. Cells expressing either scrambled, NSP4 shRNA1, or NSP4 shRNA2 are as indicated. Arrow denotes full-length, glycosylated NSP4. **(B)** Densitometry analysis of western blots for NSP4 levels normalized to that of GAPDH levels, expressed as relative to NSP4 expressed in MA104-GCaMP6s/scrambled shRNA cells. Data shown are mean ± SD of 3 infections/condition and representative of 3 independent experiments. **(C)** Plaque assay of MA104-GCaMP6s/shRNA cell lines inoculated with SA114F (10^{-6} dilution). **(D)** Representative single-cell traces of relative GCaMP6s fluorescence (F/F$_0$) from SA114F infection of cells expressing scrambled shRNA (red) or NSP4 shRNA2 (blue). **(E)** Number of Ca^{2+} spikes (F/F$_0$ > 5%) from mock or RV-infected cells inoculated with MOI0.1 SA114F. Data shown as mean ± SD of 60 cells/condition. **p<0.01.

43
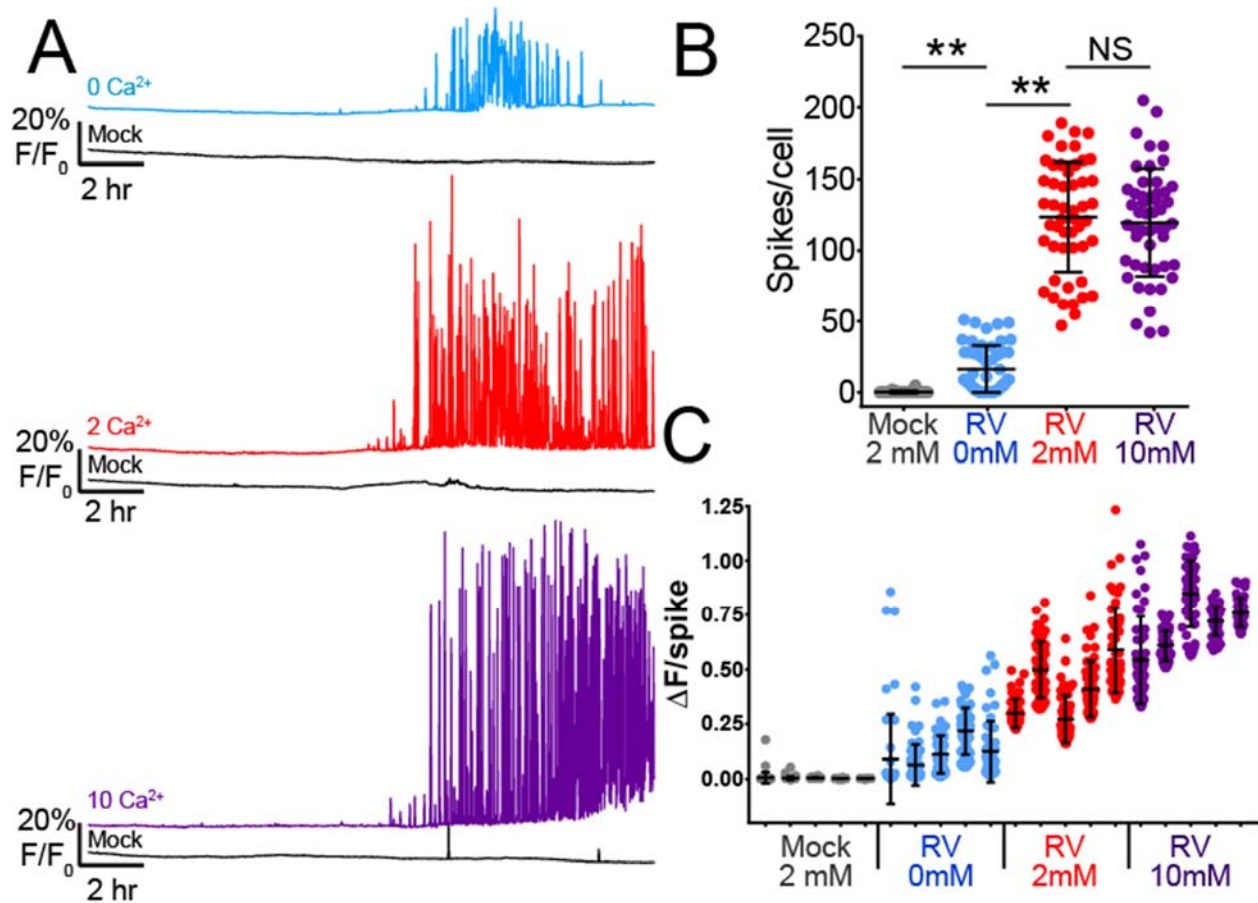
Figure 6. Ca^{2+} signaling requires extracellular Ca^{2+}. (A) Representative single-cell traces of relative GCaMP5G fluorescence (F/F$_0$) from mock (black lines) or SA114F infected cells in Ca^{2+}-free media (0Ca^{2+}, light blue), normal media (2Ca^{2+}, red), and high Ca^{2+} media (10Ca^{2+}, purple). **(B)** Number of Ca^{2+} spikes (F/F$_0$ > 5%) from mock or RV-infected cells inoculated with MOI 1 SA114F and maintained in the indicated media. Data shown as mean ± SD of 50 cells/condition. **p<0.01. **(C)** Ca^{2+} spike amplitude of the top 50 Ca^{2+} spikes from five representative mock and RV-infected cells in each media condition.
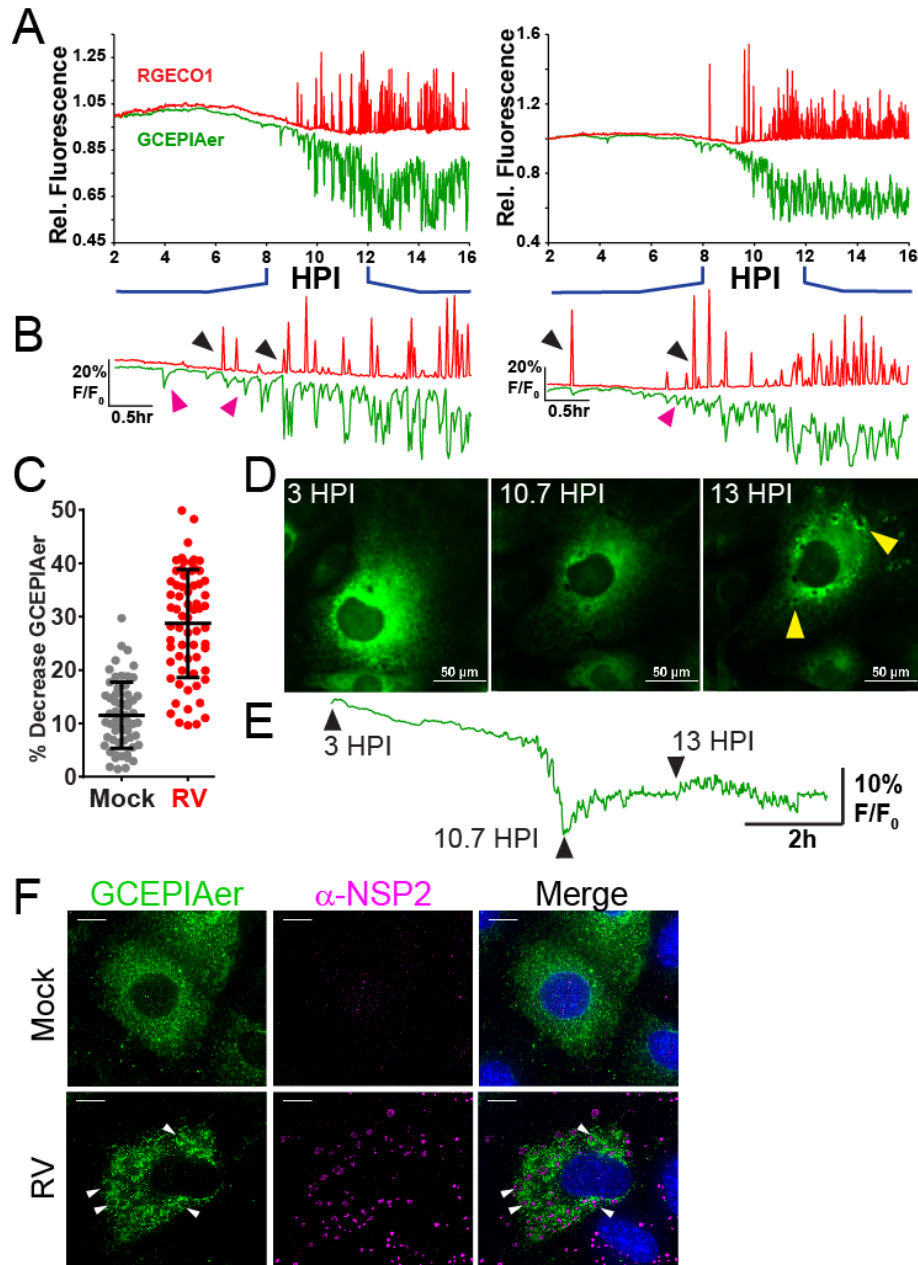
912
913 **Figure 7. RV induces dynamic decreases in ER Ca^{2+} that coincide with cytoplasmic Ca^{2+}**
914 **signals. (A)** Two representative single-cell traces of relative RGECO1.2 (red) and GCEPIAer
915 (green) fluorescence (F/F$_0$, both RGECO1.2 and GCEPIAer are shown on the same scale) from
916 MA104-RGECO/GCEPIAer cells infected with SA114F at MOI 1. **(B)** Traces from (A) expanded
917 to show details from 8-12 HPI. Black arrowheads indicate ER Ca^{2+} troughs that correspond to
918 cytoplasmic Ca^{2+} spikes. Magenta arrowheads indicate ER Ca^{2+} troughs that lack a
919 corresponding cytoplasmic Ca^{2+} spike. **(C)** Percent decrease in ER Ca^{2+} levels measured by
920 GCEPIAer fluorescence. **(D-E)** Images of a representative RV-infected MA104-GCEPIAer cell
921 (D) taken at 3, 7.75, and 10 HPI and the corresponding trace from that cell with arrowheads
922 corresponding the images above. Formation of viroplasm structures (yellow arrowheads) are
923 observed subsequent to the decrease in ER Ca^{2+} levels. **(F)** Deconvolution microscopy of mock
924 or RV-infected MA104-GCEPIAer cells (MOI 0.25, fixed 24 hpi) stained with α-NSP2 [Dylight
925 549 (pink)] to detect viroplasms (white arrowheads). (scale bar = 10 μm)

45
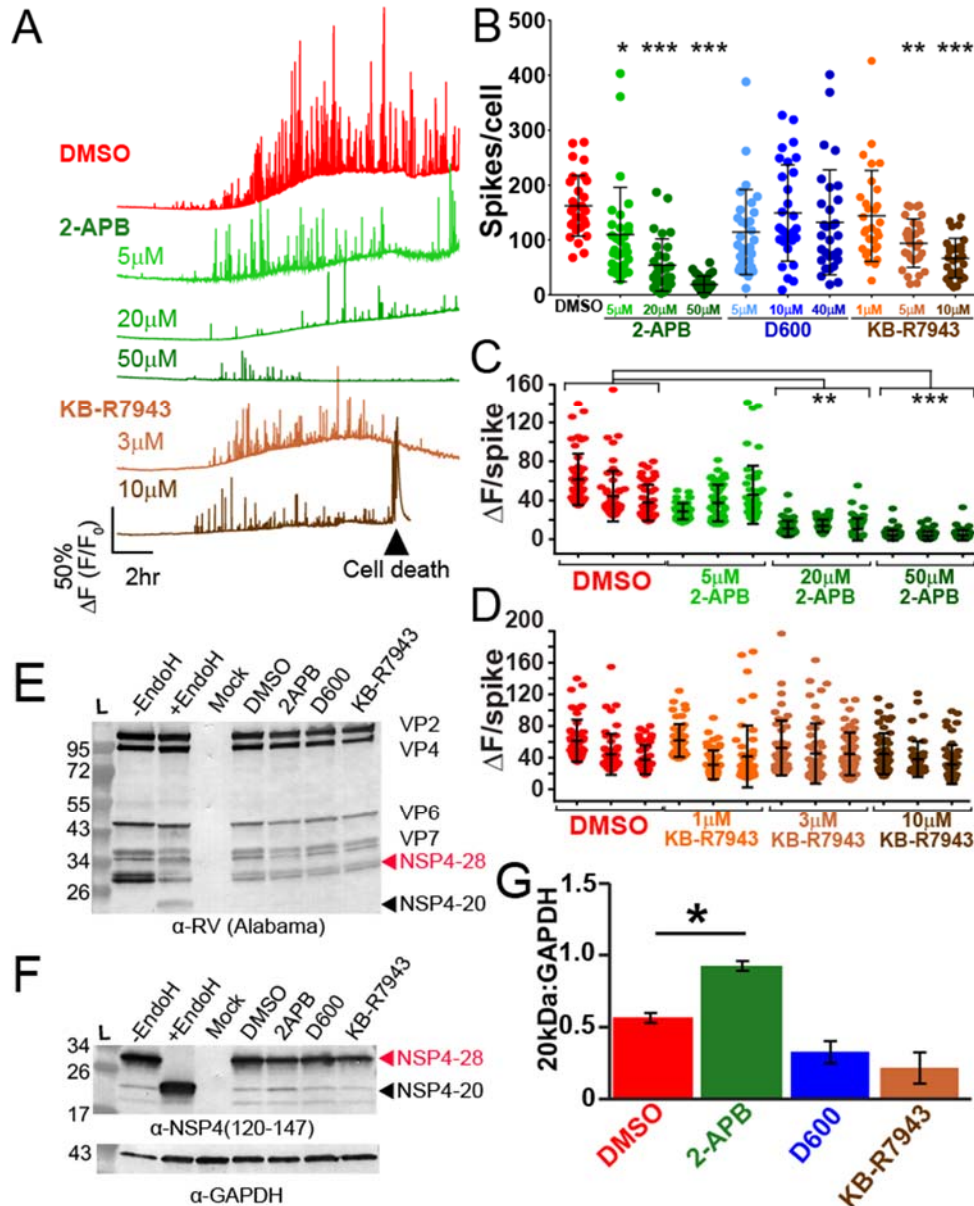
Figure 8. RV-induced Ca^{2+} signaling is blocked by the SOCE blocker 2APB. (A) Representative single-cell traces from MA104-GCaMP5G cells infected with SA114F MOI 1 and treated with DMSO vehicle alone or the indicated doses of 2APB or KB-R7943. Cell death of RV-infected cells treatment with 10 uM KB-R7943 was frequently observed (black arrowhead). **(B)** Number of Ca^{2+} spikes (F/F$_0$ > 5%) from RV-infected cells inoculated with MOI 1 and treated with the indicated concentration of 2APB, D600 or KB-R7943. **(C-D)** Ca^{2+} spike amplitude of the top 50 Ca^{2+} spikes from three representative RV-infected cells treated DMSO (vehicle) or the indicated concentration of 2APB (C) or KB-R7943 (D). **(E-F)** Western blot analysis of MA104-GCaMP5G cells mock or RV-infected MOI 1 and treated with DMSO (vehicle), 50 µM 2APB, 10 µM D600, or 10 µM KB-R7943. Control RV-infected lysates treated with Endoglycosadase H (+EndoH) or untreated (-EndoH) are also shown. Blots were detected with α-RV (E) or α-NSP4(120-147) (F) and α-GAPDH (F, bottom) was the loading control for both. **(G)** ImageJ analysis of unglycosylated NSP4 (20kDa) normalized to GAPDH from RV-infected cells treated with the different blockers. Data are the mean ± SD of three independent infections per condition. *p<0.05

46
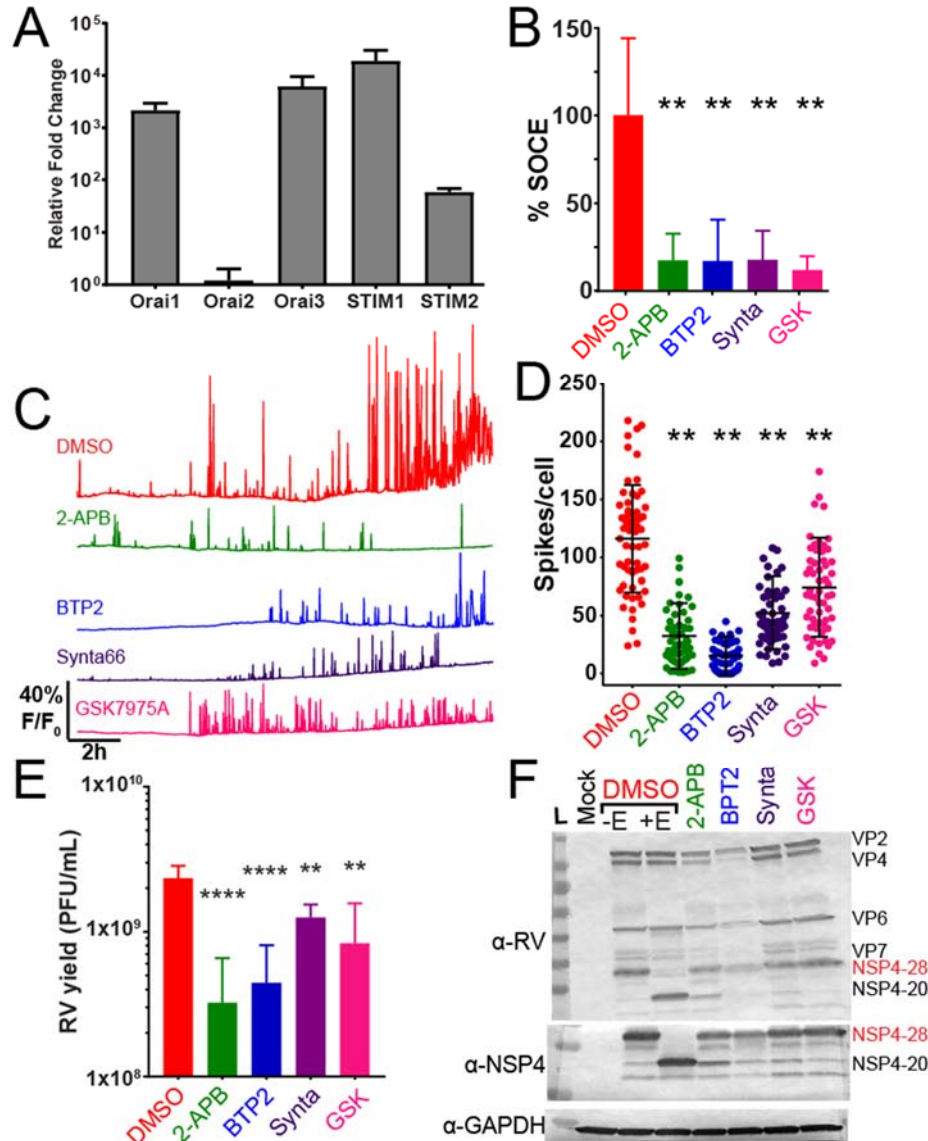
Figure 9. SOCE blockers reduce RV-induced Ca²⁺ signaling. (A) Relative mRNA expression of Orai1-3 and STIM1-2 genes in MA104 cells. Expression is normalized to 16S rRNA and graphed relative to Orai2. **(B)** SOCE was activated by treatment with 0.5 µM thapsigargin in Ca²⁺-free buffer and the amount of SOCE relative to DMSO-alone (vehicle) for different SOCE blockers determined. Data are the mean ± SD of three independent runs. **p<0.01. **(C)** Representative single-cell traces from MA104-GCaMP5G cells infected with SA114F MOI 1 and treated with DMSO vehicle alone or the indicated doses of 50 µM 2APB, 10 µM BTP2, 10 µM Synta66, or 10 µM GSK7975A. **(D)** Number of Ca²⁺ spikes (F/F₀ > 5%) from RV-infected cells inoculated with MOI 1 and treated with DMSO alone or the SOCE blockers. Data are the mean ± SD 60 cells/condition. **p<0.01 by one-way ANOVA. **(E)** SA114F yield from MA104-GCaMP5G cells treated with DMSO or the SOCE blockers. Data are the mean ± SD of three independent infections. ****p<0.0001; **p<0.01 by one-way ANOVA. **(F)** Western blot analysis of MA104-GCaMP5G cells mock or RV-infected MOI 1 and treated with DMSO or the SOCE blockers. Control RV-infected lysates treated with Endoglycosadase H (+EndoH) or untreated (-EndoH) are also shown. Blots were detected with α-RV, α-NSP4(120-147), and α-GAPDH for the loading control.
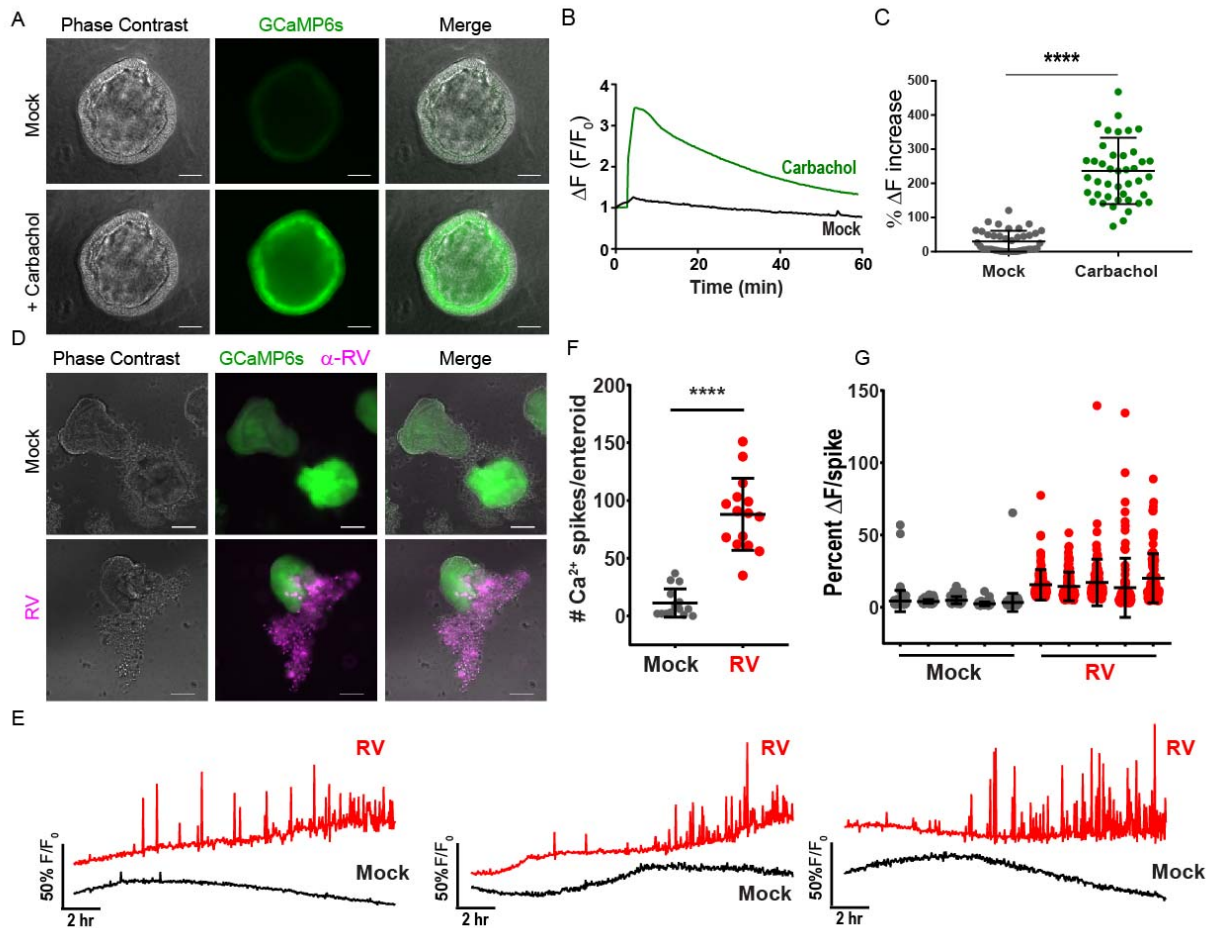
959
Figure 10. jHIE-GCaMP6s enteroids exhibit dynamic Ca^{2+} signaling during RV infection.
(A) Representative images of jejunum human intestinal enteroids stably expressing GCaMP6s (jHIE-GCaMP6s) one minute after addition of 200μM carbachol or media alone (mock). **(B)** Representative trace of jHIE-GCaMP6s treated with 200μM carbachol or media alone. GCaMP6s fluorescence (F) was normalized to the baseline fluorescence (F_0). **(C)** The maximum % increase in normalized fluorescence after addition of media (mock, N=41) or 200μM carbachol (N=43), data combined from 3 independent experiments. **(D)** Representative immunofluorescence images of mock and Ito RV-infected jHIE-GCaMP6s (green) fixed at ~24 hpi and stained for RV [Alexa Fluor 568 (pink)]. **(E)** Representative Ca^{2+} traces of whole jHIE-GCaMP6s enteroids either mock or Ito RV-infected between 6-23 hpi. GCaMP6s fluorescence (F) was normalized to the baseline fluorescence (F_0). **(F)** Number of Ca^{2+} spikes in mock (N=15) or Ito RV-infected (N=15) HIEs and **(G)** the fold change in fluorescence for randomly selected 5 HIEs mock- and RV-infected. Data are representative of one experiment that was performed in triplicate. ****p<0.0001, scale bars = 100 μm.

48
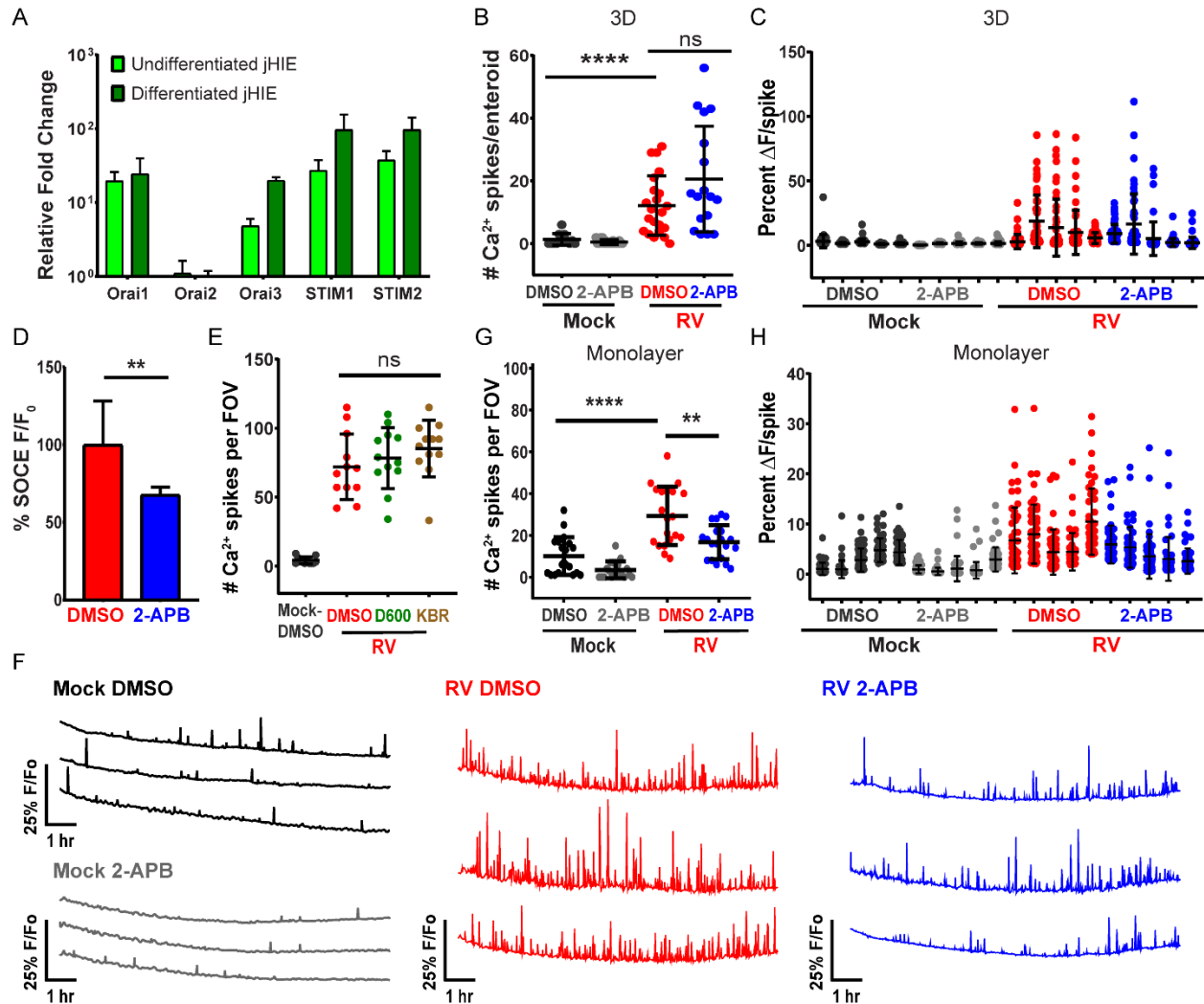
Figure 11. **Blocking SOCE reduces Ca^{2+} signaling during RV infection in jHIE-GCaMP6s monolayers. (A)** qPCR of Orai and stromal interaction molecule (STIM) mRNA transcripts normalized to 18S mRNA transcripts and fold change relative to Orai2 mRNA transcript levels in jejunum human intestinal enteroids (jHIEs), log scale (n = 3 biological replicates). **(B)** Number of Ca^{2+} spikes in 3D jHIE-GCaMP6s mock- or RV-infected and treated with DMSO (N=12, 18) or 50 μM 2APB (N=22, 17) and **(C)** the percent change in fluorescence for the highest 50 Ca^{2+} spikes for 5 HIEs of each condition for 6-18 hpi. GCaMP6s fluorescence (F) was normalized to the baseline fluorescence (F_0). Data are representative of one experiment that was performed in triplicate. **(D)** Number of Ca^{2+} spikes per field-of-view (FOV) in mock- or RV-infected jHIE-GCaMP6s monolayers treated with DMSO, 10μM D600, or 10μM KB-R7943 between 8-22 hpi, data combined from 3 experiments. **(E)** Relative fluorescence increase (F/F_0) due to store-operated calcium entry in jHIE-GCaMP6s monolayers after store depletion with 500 nM thapsigargin. Data combined from ≥6 experiments. **(F)** Representative Ca^{2+} traces per FOV of monolayers either mock- or RV-infected and treated with DMSO or 50 μM 2APB between 8-19 hpi. **(G)** Number of Ca^{2+} spikes per FOV and **(H)** the percent change in fluorescence for the highest 50 Ca^{2+} spikes for 5 FOVs of each condition for 8-19 hpi. Data combined from 5 experiments. (**p<0.01, ****p<0.0001)

49

1001   References
1002
1003   1   Hyser, J. M. & Estes, M. K. Pathophysiological Consequences of Calcium-Conducting
1004   Viroporins. *Annu. Rev. Virol* **2**, 473-496, doi:10.1146/annurev-virology-100114-054846
1005   [doi] (2015).
1006   2   Troeger, C. *et al.* Rotavirus Vaccination and the Global Burden of Rotavirus Diarrhea
1007   Among Children Younger Than 5 Years. *JAMA Pediatr* **172**, 958-965,
1008   doi:10.1001/jamapediatrics.2018.1960 (2018).
1009   3   Thiagarajah, J. R., Donowitz, M. & Verkman, A. S. Secretory diarrhoea: mechanisms
1010   and emerging therapies. *Nat. Rev. Gastroenterol. Hepatol* **12**, 446-457,
1011   doi:nrgastro.2015.111 [pii];10.1038/nrgastro.2015.111 [doi] (2015).
1012   4   Michelangeli, F., Ruiz, M. C., del Castillo, J. R., Ludert, J. E. & Liprandi, F. Effect of
1013   rotavirus infection on intracellular calcium homeostasis in cultured cells. *Virology* **181**,
1014   520-527 (1991).
1015   5   Sastri, N. P., Crawford, S. E. & Estes, M. K. in *Viral Gastroenteritis: Molecular*
1016   *Epidemiology and Pathogenesis* (eds L. Svensson, U. Desselberger, H.B. Greenberg, &
1017   M.K. Estes) Ch. 2.4, 145-174 (Elsevier Academic Press, 2016).
1018   6   Tian, P. *et al.* The rotavirus nonstructural glycoprotein NSP4 mobilizes Ca2+ from the
1019   endoplasmic reticulum. *J Virol* **69**, 5763-5772 (1995).
1020   7   Diaz, Y. *et al.* Expression of nonstructural rotavirus protein NSP4 mimics Ca2+
1021   homeostasis changes induced by rotavirus infection in cultured cells. *J Virol* **82**, 11331-
1022   11343 (2008).
1023   8   Hyser, J. M., Collinson-Pautz, M. R., Utama, B. & Estes, M. K. Rotavirus disrupts
1024   calcium homeostasis by NSP4 viroporin activity. *mBio* **1**, e00265-00210 (2010).
1025   9   Pham, T., Perry, J. L., Dosey, T. L., Delcour, A. H. & Hyser, J. M. The Rotavirus NSP4
1026   Viroporin Domain is a Calcium-conducting Ion Channel. *Sci Rep* **7**, 43487,
1027   doi:10.1038/srep43487 (2017).
1028   10   Hyser, J. M., Utama, B., Crawford, S. E., Broughman, J. R. & Estes, M. K. Activation of
1029   the endoplasmic reticulum calcium sensor STIM1 and store-operated calcium entry by
1030   rotavirus requires NSP4 viroporin activity. *J Virol* **87**, 13579-13588 (2013).
1031   11   Diaz, Y. *et al.* Dissecting the Ca(2)(+) entry pathways induced by rotavirus infection and
1032   NSP4-EGFP expression in Cos-7 cells. *Virus. Res* **167**, 285-296 (2012).
1033   12   Perez, J. F., Ruiz, M. C., Chemello, M. E. & Michelangeli, F. Characterization of a
1034   membrane calcium pathway induced by rotavirus infection in cultured cells. *J Virol* **73**,
1035   2481-2490 (1999).
1036   13   Zhang, M., Zeng, C. Q., Morris, A. P. & Estes, M. K. A functional NSP4 enterotoxin
1037   peptide secreted from rotavirus-infected cells. *J Virol* **74**, 11663-11670 (2000).
1038   14   Dong, Y., Zeng, C. Q., Ball, J. M., Estes, M. K. & Morris, A. P. The rotavirus enterotoxin
1039   NSP4 mobilizes intracellular calcium in human intestinal cells by stimulating
1040   phospholipase C-mediated inositol 1,4,5-trisphosphate production. *Proc. Natl. Acad. Sci.*
1041   *U. S. A* **94**, 3960-3965 (1997).
1042   15   Ball, J. M., Tian, P., Zeng, C. Q., Morris, A. P. & Estes, M. K. Age-dependent diarrhea
1043   induced by a rotaviral nonstructural glycoprotein. *Science* **272**, 101-104 (1996).
1044   16   Morris, A. P. *et al.* NSP4 elicits age-dependent diarrhea and Ca(2+)mediated I(-) influx
1045   into intestinal crypts of CF mice. *Am. J Physiol* **277**, G431-G444 (1999).
1046   17   Ousingsawat, J. *et al.* Rotavirus toxin NSP4 induces diarrhea by activation of TMEM16A
1047   and inhibition of Na+ absorption. *Pflugers. Arch* **461**, 579-589 (2011).
1048   18   Perez, J. F., Chemello, M. E., Liprandi, F., Ruiz, M. C. & Michelangeli, F. Oncosis in
1049   MA104 cells is induced by rotavirus infection through an increase in intracellular Ca2+
1050   concentration. *Virology* **252**, 17-27 (1998).

51

1051   19   Brunet, J. P. *et al.* Rotavirus infection induces an increase in intracellular calcium
1052   concentration in human intestinal epithelial cells: role in microvillar actin alteration. *J*
1053   *Virol* **74**, 2323-2332 (2000).
1054   20   Tanwar, J. & Motiani, R. K. Role of SOCE architects STIM and Orai proteins in Cell
1055   Death. *Cell Calcium* **69**, 19-27, doi:S0143-4160(17)30059-3
1056   [pii];10.1016/j.ceca.2017.06.002 [doi] (2018).
1057   21   Soboloff, J., Rothberg, B. S., Madesh, M. & Gill, D. L. STIM proteins: dynamic calcium
1058   signal transducers. *Nat Rev Mol Cell Biol* **13**, 549-565 (2012).
1059   22   Zambrano, J. L. *et al.* Silencing of rotavirus NSP4 or VP7 expression reduces alterations
1060   in Ca2+ homeostasis induced by infection of cultured cells. *J Virol* **82**, 5815-5824 (2008).
1061   23   Perry, J. L., Ramachandran, N. K., Utama, B. & Hyser, J. M. Use of genetically-encoded
1062   calcium indicators for live cell calcium imaging and localization in virus-infected cells.
1063   *Methods* **90**, 28-38, doi:S1046-2023(15)30075-X [pii];10.1016/j.ymeth.2015.09.004 [doi]
1064   (2015).
1065   24   Suzuki, J. *et al.* Imaging intraorganellar Ca2+ at subcellular resolution using CEPIA. *Nat.*
1066   *Commun* **5**, 4153, doi:ncomms5153 [pii];10.1038/ncomms5153 [doi] (2014).
1067   25   Bialowas, S. *et al.* Rotavirus and Serotonin Cross-Talk in Diarrhoea. *PLoS One* **11**,
1068   e0159660, doi:10.1371/journal.pone.0159660 [doi];PONE-D-16-05251 [pii] (2016).
1069   26   Saxena, K. *et al.* Human Intestinal Enteroids: a New Model To Study Human Rotavirus
1070   Infection, Host Restriction, and Pathophysiology. *J Virol* **90**, 43-56, doi:JVI.01930-15
1071   [pii];10.1128/JVI.01930-15 [doi] (2015).
1072   27   Kanai, Y. *et al.* Entirely plasmid-based reverse genetics system for rotaviruses. *Proc Natl*
1073   *Acad Sci U S A* **114**, 2349-2354, doi:10.1073/pnas.1618424114 (2017).
1074   28   Philip, A. A. H., B. E.; Garcia, M. L.; Abad, A. T.; Katen, S. P.; Patton, J. T. Collection of
1075   recombinant rotaviruses expressing fluorescent reporter proteins. *Microbiol Resour*
1076   *Announc* (2019).
1077   29   Crawford, S. E., Hyser, J. M., Utama, B. & Estes, M. K. Autophagy hijacked through
1078   viroporin-activated calcium/calmodulin-dependent kinase kinase-beta signaling is
1079   required for rotavirus replication. *Proc Natl Acad Sci U. S. A* **109**, E3405-E3413 (2012).
1080   30   Criglar, J. M. *et al.* A novel form of rotavirus NSP2 and phosphorylation-dependent
1081   NSP2-NSP5 interactions are associated with viroplasm assembly. *J Virol* **88**, 786-798,
1082   doi:10.1128/JVI.03022-13 (2014).
1083   31   Hyser, J. M., Zeng, C. Q., Beharry, Z., Palzkill, T. & Estes, M. K. Epitope mapping and
1084   use of epitope-specific antisera to characterize the VP5* binding site in rotavirus SA11
1085   NSP4. *Virology* **373**, 211-228 (2008).
1086   32   Chang-Graham, A. L. *et al.* Human intestinal enteroids with inducible neurogenin-3
1087   expression as a novel model of gut hormone secretion. *bioRxiv*, 579698,
1088   doi:10.1101/579698 (2019).
1089   33   Sato, T. *et al.* Long-term expansion of epithelial organoids from human colon, adenoma,
1090   adenocarcinoma, and Barrett's epithelium. *Gastroenterology* **141**, 1762-1772 (2011).
1091   34   Chang-Graham, A. L. *et al.* Human intestinal enteroids with inducible neurogenin-3
1092   expression as a novel model of gut hormone secretion. *Cell Mol Gastroenterol Hepatol*,
1093   doi:10.1016/j.jcmgh.2019.04.010 (2019).
1094   35   Ettayebi, K. *et al.* Replication of human noroviruses in stem cell-derived human
1095   enteroids. *Science* **353**, 1387-1393, doi:science.aaf5211 [pii];10.1126/science.aaf5211
1096   [doi] (2016).
1097   36   VanDussen, K. L. *et al.* Development of an enhanced human gastrointestinal epithelial
1098   culture system to facilitate patient-based assays. *Gut* **64**, 911-920, doi:10.1136/gutjnl-
1099   2013-306651 (2015).
1100   37   Estes, M. K., Graham, D. Y., Gerba, C. P. & Smith, E. M. Simian rotavirus SA11
1101   replication in cell cultures. *J Virol* **31**, 810-815 (1979).

1102   38   Matrosovich, M., Matrosovich, T., Garten, W. & Klenk, H. D. New low-viscosity overlay
1103   medium for viral plaque assays. *Virol J* **3**, 63, doi:10.1186/1743-422X-3-63 (2006).
1104   39   del Castillo, J. R. *et al.* Rotavirus infection alters Na+ and K+ homeostasis in MA-104
1105   cells. *J Gen. Virol* **72 (Pt 3)**, 541-547 (1991).
1106   40   Zhang, M. *et al.* Mutations in rotavirus nonstructural glycoprotein NSP4 are associated
1107   with altered virus virulence. *J Virol* **72**, 3666-3672 (1998).
1108   41   Zhao, Y. *et al.* An expanded palette of genetically encoded Ca(2)(+) indicators. *Science*
1109   **333**, 1888-1891, doi:science.1208592 [pii];10.1126/science.1208592 [doi] (2011).
1110   42   Shahrabadi, M. S., Babiuk, L. A. & Lee, P. W. Further analysis of the role of calcium in
1111   rotavirus morphogenesis. *Virology* **158**, 103-111 (1987).
1112   43   Motiani, R. K., Stolwijk, J. A., Newton, R. L., Zhang, X. & Trebak, M. Emerging roles of
1113   Orai3 in pathophysiology. *Channels. (Austin.)* **7**, 392-401, doi:24960
1114   [pii];10.4161/chan.24960 [doi] (2013).
1115   44   Foulke-Abel, J. *et al.* Human enteroids as an ex-vivo model of host-pathogen
1116   interactions in the gastrointestinal tract. *Exp. Biol Med (Maywood.)* **239**, 1124-1134,
1117   doi:1535370214529398 [pii];10.1177/1535370214529398 [doi] (2014).
1118   45   Zachos, N. C. *et al.* Human Enteroids/Colonoids and Intestinal Organoids Functionally
1119   Recapitulate Normal Intestinal Physiology and Pathophysiology. *J Biol Chem* **291**, 3759-
1120   3766, doi:R114.635995 [pii];10.1074/jbc.R114.635995 [doi] (2016).
1121   46   Zhou, Y., Frey, T. K. & Yang, J. J. Viral calciomics: interplays between Ca2+ and virus.
1122   *Cell Calcium* **46**, 1-17 (2009).
1123   47   Bhowmick, R. *et al.* Rotaviral enterotoxin nonstructural protein 4 targets mitochondria for
1124   activation of apoptosis during infection. *J Biol Chem* **287**, 35004-35020 (2012).
1125   48   Dickman, K. G. *et al.* Rotavirus alters paracellular permeability and energy metabolism in
1126   Caco-2 cells. *Am J Physiol Gastrointest Liver Physiol* **279**, G757-766,
1127   doi:10.1152/ajpgi.2000.279.4.G757 (2000).
1128   49   Zhu, S. *et al.* Nlrp9b inflammasome restricts rotavirus infection in intestinal epithelial
1129   cells. *Nature* **546**, 667-670, doi:10.1038/nature22967 (2017).
1130   50   Zambrano, J. L. *et al.* Rotavirus infection of cells in culture induces activation of RhoA
1131   and changes in the actin and tubulin cytoskeleton. *PLoS One* **7**, e47612,
1132   doi:10.1371/journal.pone.0047612 [doi];PONE-D-12-19556 [pii] (2012).
1133   51   Hagbom, M. *et al.* Rotavirus stimulates release of serotonin (5-HT) from human
1134   enterochromaffin cells and activates brain structures involved in nausea and vomiting.
1135   *PLoS Pathog* **7**, e1002115 (2011).
1136   52   Ruiz, M. C. *et al.* Ca2+ permeability of the plasma membrane induced by rotavirus
1137   infection in cultured cells is inhibited by tunicamycin and brefeldin A. *Virology* **333**, 54-65
1138   (2005).
1139   53   Crawford, S. E. & Desselberger, U. Lipid droplets form complexes with viroplasms and
1140   are crucial for rotavirus replication. *Curr. Opin Virol* **19**, 11-15, doi:S1879-
1141   6257(16)30059-1 [pii];10.1016/j.coviro.2016.05.008 [doi] (2016).
1142